

Deep residual network based fault detection and diagnosis of photovoltaic arrays using current-voltage curves and ambient conditions

Zhicong Chen^{a,b}, Yixiang Chen^{a,b}, Lijun Wu^{a,b,*}, Shuying Cheng^{a,b,*}, Peijie Lin^{a,b}

^a College of Physics and Information Engineering, Fuzhou University, 2 XueYuan Road, 350116 Fuzhou, China

^b Jiangsu Collaborative Innovation Centre of Photovoltaic Science and Engineering, 213164 Changzhou, China

ARTICLE INFO

Keywords:

Photovoltaic arrays
Fault detection and diagnosis
Current-voltage characteristic curves
Deep residual networks
Deep learning

ABSTRACT

Automatic fault detection and diagnosis techniques for photovoltaic arrays are crucial to promote the efficiency, reliability and safety of photovoltaic systems. In recent decades, many conventional artificial intelligence approaches have been successfully applied to automatically establish fault detection and diagnosis model using fault data samples, but most of them rely on manual feature extraction or expert knowledge to build diagnosis models, which is inefficient and may ignore some potential useful features. In addition, they usually use shallow neural networks with limited performance. Addressing the issues, this paper proposes a novel intelligent fault detection and diagnosis method for photovoltaic arrays based on a newly designed deep residual network model trained by the adaptive moment estimation deep learning algorithm, which can automatically extract features from raw current-voltage curves and ambient irradiance and temperature, and effectively improve the performance with a deeper network. In order to validate the proposed fault diagnosis model, a Simulink based simulation model is designed for a real laboratory photovoltaic array, and both fault simulation and real experiments are carried out to obtain simulation and experimental fault datasets. Furthermore, two other popular deep learning based models are used for comparison, including convolution neural network and convolutional auto-encoder. Both of simulation and real experimental comparison results demonstrate that the proposed deep residual network based method achieves high and best overall performance in terms of accuracy, generalization performance, reliability and training efficiency.

1. Introduction

With oncoming shortage of the fossil energy and deterioration of environment pollution, there is an urgent need for sustainable and clean energy sources to satisfy the increasing demand of energy consumption and environment protection. Among various renewable energy sources, the solar energy has been drawing more and more attention because of the sustainability, cleanness and broad availability, and photovoltaic (PV) power generation is the main way to exploit solar energy. According to the International Energy Agency (IEA) latest report, global accumulative installed capacity of photovoltaic power systems has experienced exponential growth in the last decades and reached at least 505 Giga Watts by the end of 2018, in which 99.8 Giga Watts of PV power systems were installed worldwide in 2018 [1]. As the fundamental components of photoelectric energy conversion, PV arrays are composed of a large number of PV modules and complex cabling, and they commonly operate in harsh outdoor environments. Due to many potential factors (such as corrosion, strong wind, heavy rain, hail,

soiling, ultraviolet exposure, thermal cycling, rodent chewing, possible inappropriate transportation/installation/maintenance, etc.), they are prone to suffering from various types and levels of faults or abnormality [2], such as short-circuit (line-line and line to ground) faults [3], partial shading [4], aging degradation [5], open-circuit fault [6], DC arc fault [7], hot spot [8], potential induced degradation (PID) [9], micro-crack [10], and so on. To protect PV systems from catastrophic events, some conventional protection devices are commonly installed on the DC-side PV arrays [11], such as over current protection device (OCPD), ground fault detection and interrupter (GFDI), arc fault circuit interrupter (AFCI) and so on. However, early minor faults with low mismatch or high impedance remain unprotected and are difficult and time consuming to be detected manually, which may cause the reduction of the power generation efficiency and degradation of the system and even deteriorate fire disasters [12]. Therefore, automatic fault detection and diagnosis (FDD) technologies are essential to detect these early faults for efficient, reliable and safe operation and maintenance of PV power plants, which are attracting more and more research interest from the

* Corresponding authors at: College of Physics and Information Engineering, Fuzhou University, 2 XueYuan Road, 350116 Fuzhou, China.
E-mail address: lijun.wu@fzu.edu.cn (L. Wu).

academic and industrial communities in recent years [13].

In the last decade, various FDD techniques have been put forward for PV arrays. In terms of the sensing principle, the reported fault diagnosis methods includes thermal imaging [14], electroluminescence (EL) imaging [15], earth capacitance measurement (ECM) [16], time domain reflectometry (TDR) [17], and electrical characteristics monitoring [18]. Thermal imaging methods rely on infrared (IR) camera to acquire the thermal images radiated by PV modules in real operating conditions. Although they can efficiently detect hot spot faults of solar cell level, but the reliability is strongly affected by the sunlight. Instead, EL methods actively apply a forward bias voltage on PV modules and then use camera to acquire the light emitted by solar cells. Micro-crack or defects of internal solar cells of PV modules can be easily observed from EL images, but external power supply is needed and the PV modules should be moved into a dark room. The ECM method was proposed by Takashima et al. [19] and used to detect and locate the disconnection in a PV string by measuring the earth capacitance and then comparing the values of normal string and potentially faulty string. TDR methods were used to detect and locate impedance change caused by aging or ground faults, through inputting special signal into PV strings and measuring the reflected signal for the comparison between normal and faulty strings [17]. Both of the ECM and TDR methods can realize fault location and are insensitive to irradiance, but the ECM is dedicated for detecting open-circuit while the TDR is only for detecting impedance change. According to the literature, the electrical characteristics methods are the dominant, which can detect, classify and locate various types of faults directly using electrical parameters (voltage, current, power and I-V curves) together with ambient conditions (irradiance and temperature) [20]. This study focuses on the electrical characteristics based methods. From the perspective of fault diagnosis principle, electrical characteristics based methods could be further classified into physical model and/or signal processing based threshold methods and data and/or rule based artificial intelligent (AI) methods [21].

Threshold based FDD methods commonly rely on manual extraction and analysis of fault indicators for determining the procedure and threshold to judge the faulty status. Firstly, some indicators sensitive to faults were extracted from measured electrical data and their theoretical values calculated by physical model and measured ambient conditions, such as power loss with voltage/current ratios [22], normalized voltage and current [23], operating voltage waveform [24], operating voltage window [25], slopes of normalized power curve [26], power/voltage/current indicators [27], normalized difference of DC power/voltage [28], seven indicators (current and voltage at maximum power points, short-circuit current, open-circuit voltage, series resistance, filled factor, and thermal voltage) [29], model parameters extracted from I to V curves [30], derivative of I-V curve error to voltage [31], and so on. Based on analysis of extracted indicators, fault detection procedures were then proposed by comparing the indicators with pre-determined thresholds. To alleviate the impact of measurement noise and exploit the temporal properties, various signal processing techniques were also applied on the time series of monitored data for fault detection, such as exponentially weighted moving average chart [32] and its variants [33], statistical analysis by t-test [34] and local likelihood ratio test [35], wavelet packet [36], Kalman filter [37], and so on. Aforementioned threshold based FDD algorithms were all proved to be efficient and effective, but the manual extraction of fault indicators and determination of corresponding thresholds are time consuming, and the generalization performance is limited. Furthermore, the performance of fault detection may be greatly affected by the accuracy of PV models, and the capability to diagnose different faults is quite limited.

In the recent decade, various AI based FDD methods were proposed for PV arrays as well to address the issues of traditional threshold based methods, which utilize abundant data samples or expert knowledge to automatically build accurate fault diagnosis models [38]. In the

literature, there are mainly three classes of AI techniques used for FDD of PV arrays, including machine learning (ML), fuzzy inference system (FIS) and their hybrid. Many conventional ML algorithms have been explored and applied for FDD of PV arrays. These ML based FDD methods commonly use abundant data samples to automatically build up black-box FDD models, which can be further categorized into supervised, semi-supervised and unsupervised methods. Supervised ML based FDD methods rely on labeled data samples to build up the models. There are many supervised ML algorithms used for FDD of PV arrays, such as decision trees (DT) [39], random forest [21], artificial neural networks (ANN) [40], support vector machine (SVM) [41], extreme learning machine (ELM) [42], probabilistic neural network (PNN) [43], and so on. Although supervised ML based methods can build up reliable and accurate FDD models, it is costly to obtain a large number of labeled data. Instead, semi-supervised ML methods only require a small amount of labeled data, while unsupervised ML methods even just need unlabeled data samples. Several semi-supervised and unsupervised ML algorithms for FDD of PV arrays were proposed, including graph-based semi-supervised learning [44], density peak based clustering [45], K-means clustering [46], unsupervised clustering with PNN [47], and dilation and erosion based clustering [48]. But, the accuracy is strongly affected by the distribution of the data samples. Different from ML methods, FIS based methods rely on linguistic fuzzy sets and fuzzy rules obtained from expert experience to quickly establish the FDD model [49], which can perform human-alike inference based fault detection and classification [50]. Combining the advantages of ML and FIS algorithms, some hybrid AI methods were used for FDD of PV arrays, including Fuzzy C-mean clustering [51], adaptive neuro-fuzzy classifier [52]. Although these ML and/or FIS methods can build effective FDD models automatically, they still rely on the fault features that are manually extracted from raw data based on rigorous analysis of faults impact, which would compromise the modeling efficiency and ignore some potential useful features leading to limited performance.

With the fast improvement of microprocessors performance, especially parallel computing techniques (such as the CUDA platform provided by the NVIDIA incorporate), the computation capability of computers is rapidly increasing, greatly supporting the prosperity of complex AI techniques in recent years. Particularly, the deep learning (DL) techniques based deep neural networks (DNN) are quickly emerging and are being applied successfully for more and more civil and industrial applications, such as image classification, object recognition and tracking, medical diagnosis, and so on [53]. In contrast to conventional shallow ML algorithms, most DL based DNNs can achieve a higher performance through deeper network structures and automatically learn complex features with abstract representation directly from raw data, which can overcome the drawbacks of shallow ML algorithms [54]. Several DL algorithms have been applied in the fault diagnosis of other topics (e.g., mechanical machines) [55], such as convolutional neural network (CNN) [56], sparse auto-encoder [57], deep belief network (DBN) [58], and so on. Recently, some DL algorithms were proposed for fault diagnosis of PV system, such as CNN [59], long short term machine (LSTM) [60]. Theoretically, although deeper networks may produce a higher performance, they are more difficult to train and tend to suffer from gradient vanishing or explosion, leading to slow convergence and overfitting issues [61]. In order to solve these shortcomings, the deep residual networks (ResNet) with shortcut connections among hidden layers firstly proposed by He et al. [62] are emerging, which can improve the training efficiency and accuracy for deeper networks. The ResNet was successfully applied on the fault diagnosis of gearbox and proved to be better than other DL algorithms [63], and it was applied by the authors for accurate modeling of PV modules as well [64].

In view of the advantages of DL techniques, especially of the ResNet structure, this study focuses on DL based fault detection and diagnosis of the DC-side PV arrays of PV systems. The main contributions are summarized in the following aspects:

- (1) A new two-dimensional ResNet structure is designed and applied for building the FDD model of PV arrays using the raw data of I-V characteristics curves and ambient conditions. The proposed ResNet consists of residual blocks, convolutional layers, average pooling layers and linear classifier.
- (2) Original measured I-V characteristics curves of various conditions are down-sampled by bilinear interpolation to reduce the data dimension, and then they are combined with corresponding irradiance and temperature to form two-dimensional data samples for training the ResNet based model
- (3) A Simulink based PV array model is built for a laboratory small scale PV array to simulate some common early faults at arbitrary ambient conditions for verifying the ResNet base FDD model. Based on the simulation model, the impact of various faults on I-V characteristics curves are analyzed to show the possibility of fault classification from the curve shape.
- (4) Different types and levels of early faults experiments are carried out on the small scale PV array and Simulink based model to obtain the I-V curves and corresponding irradiance and temperature under different ambient conditions. Then, the proposed ResNet based FDD model is trained and tested based on the simulated and real data samples. Both simulation and real experiments results validate that the proposed ResNet based FDD model features high accuracy, reliability and generalization performance.
- (5) Two other state-of-the-art DNNs, including CNN and convolutional auto-encoder (CAE), are tested as well for comparison with the proposed ResNet. The comparison results demonstrate the proposed ResNet based FDD model achieves the best accuracy, generalization, reliability and training efficiency.

The remainder of this paper is structured as follows. Section 2 describes the Simulink based PV arrays model and the simulation of various faults, and analyzes the impact of the faults on I-V curves. In Section 3, the new ResNet structure and the learning algorithm are detailed, and then the procedure to build the ResNet based FDD model is depicted. Fault experiments are carried out to obtain the simulation and real datasets in Section 4, based on which the ResNet based FDD method is validated. Lastly, some significant conclusions are drawn.

2. Modeling and analysis of early photovoltaic array faults

In this section, an accurate modeling method of a real PV array testing system is firstly introduced. Then, the simulation method of some common early faults under various ambient conditions is described. Lastly, the fault simulation is carried out to study the impact of the faults on the output I-V characteristics curves of the PV array. But, the experimental setup of the real PV array and the testing system will be detailed in Section 4.

2.1. Modeling of a real photovoltaic array

In order to validate the proposed FDD method, a small scale laboratory PV array system and corresponding Simulink based PV model are firstly built as shown in Fig. 1. The PV system model is designed to conduct PV array fault simulation with controllable irradiance and temperature, and to obtain corresponding I-V characteristic and ambient conditions. The PV system model use a voltage source controlled by a ramp signal for simulating a real I-V tester as illustrated in Fig. 1(a). The PV array consists of eighteen monocrystalline silicon PV modules (Model: GL-100) configured into three PV strings in parallel with six PV modules (PVM) in each string. Especially, the broadly used efficient single diode model (SDM) is adopted to model the PV modules, the Simulink equivalent circuit of which is illustrated in Fig. 1(b) and (c). Specifically, the SDM model equation for the basic solar cell is defined by Eq. (1). Since a PV module is composed of identical solar cells in series and/or in parallel, the model equation of the PV module

can be described by Eq. (2), assuming that the terminal voltage and current are uniformly distributed into the solar cells [65].

$$I = I_{ph} - I_s \left[\exp\left(\frac{q(V + IR_s)}{nKT} - 1\right) - \frac{V + IR_s}{R_{sh}} \right] \quad (1)$$

$$I / N_p = I_{ph} - I_s \left[\exp\left(\frac{q(V/N_s + IR_s/N_p)}{nKT} - 1\right) - \frac{V/N_s + IR_s/N_p}{R_{sh}} \right] \quad (2)$$

In Eqs. (1) and (2), there are five model parameters to be identified, including the photocurrent (I_{ph}), diode ideality factor (n), saturation current (I_s), series resistance (R_s) and shunt resistance (R_{sh}); The constant q represents the absolute value of electron charge (1.60218×10^{-19} C) and K is the Boltzman constant (1.38065×10^{-23} J/K); N_s and N_p are the number of solar cells in series and cell strings in parallel of a PV module respectively; T is the solar cell absolute temperature. Generally, internal model parameters mainly vary with the operating conditions, including the irradiance and temperature. In the proposed model, the I_{ph} is configured to vary with the temperature and irradiance by the Eq. (3), while other parameters are configured to be fixed for improving the model efficiency.

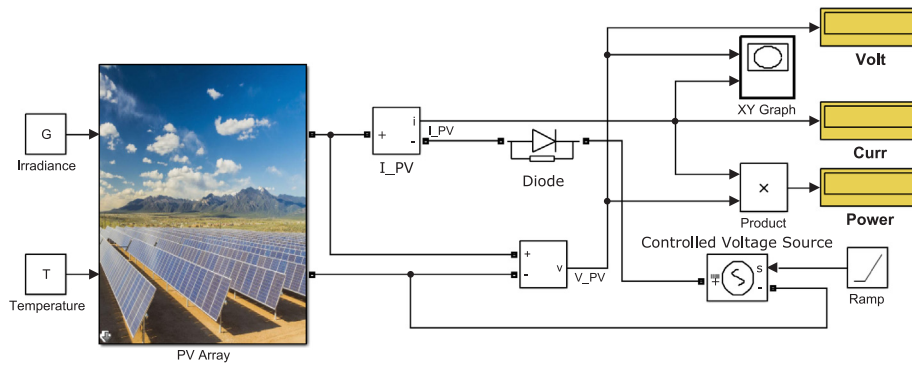
$$I_{ph} = [I_{ph,STC} + \alpha(T - T_{STC})] \cdot \frac{G}{G_{STC}} \quad (3)$$

where the $I_{ph,STC}$ represents the values of five model parameters at the STC condition; The T , G , T_{STC} , and G_{STC} are the temperature and irradiance of operating condition (OPC) and standard test condition (STC condition) respectively; In addition, the α is the temperature coefficient of the photocurrent (I_{ph}).

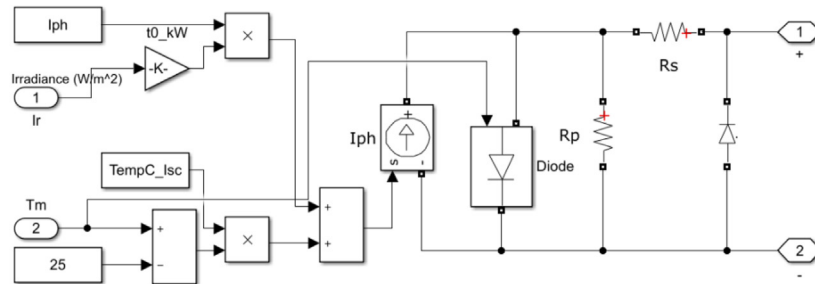
Based on the SDM equivalent circuit, many parameters identification techniques were proposed to extract the five parameters from I to V curves or rated data of PV modules provided by manufacturer [66]. In this study, the parameter extraction methods proposed in [67] were used to extract the five STC model parameters from the rated data of the PV module, including short-circuit current, open-circuit voltage, and the maximum power point (MPP) voltage and current at STC. The rated data of the GL-100 PV module and the extracted parameters are given in Table 1. To verify the model, some I-V and P-V curves under different irradiance and temperature are obtained from the model as shown in Fig. 2, and it can be observed that they are basically in accordance with the rated data of the PV module provided by the manufacturer, especially with the temperature coefficients.

2.2. Simulation and analysis of early photovoltaic array faults

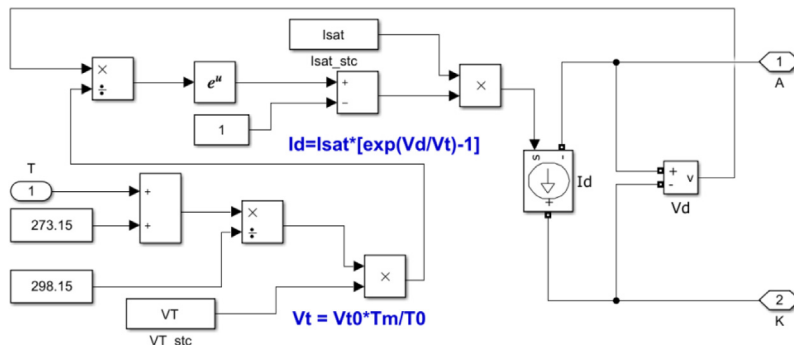
Four types of common early faults are investigated in this paper, including short-circuit faults, open circuit faults, degradation faults, and partial shading. Short-circuit faults represent accidental connection or low-impedance among two points in a PV array [11], which may be caused by insulation damage of cables (due to corrosion, rodent chewing, water leakage, aging, etc.), PV module internal damage, misoperation during installation or maintenance, etc. Short-circuit faults can be further classified into line-line and line-ground faults, and they would lead to a large reverse current flow that obviously reduce power output and even results in electric shock and fire disaster. Open-circuit faults refer to the disconnection of cables or connector, the causes of which are similar to short-circuit faults and they mainly lead to power losses. Degradation faults refer to the accidental aging of PV modules, connectors and/or cables, which may be caused by corrosion, ultraviolet exposure, and so on. Degradation faults commonly result in increase of the equivalent series resistance or decrease of the parallel resistance, which would mainly lead to significant decrease of power. Partial shading mainly refers to partly different irradiance input of PV modules in a PV array (due to soiling, dirt, leaves, obstruction by buildings, trees and so on) [68], which may cause power losses and hot spots in PV modules.



(a) Simulation circuit for I-V testing of the PV array



(b) Model of the PV module



(c) Model of the diode in the PV module model

Fig. 1. Simulink based simulation model of the PV array.

Table 1
Specification for GL-100 PV module of monocrystalline silicon.

Rated data	Value	Extracted parameters	Value
P _{mpp} (W)	100	I _{s,STC} (A)	0.18e-6
V _{oc} (V)	21.5	I _{ph,STC} (A)	6.038
I _{sc} (A)	6.03	n _{STC}	48.3
V _{mpp} (V)	17.5	R _{s,STC} (Ω)	0.1
I _{mpp} (A)	5.71	R _{sh,STC} (Ω)	644.3
Solar cell number in series	36		
Temperature coefficient of I _{sc}	0.06%/K		
Temperature coefficient of V _{oc}	-78 mV/K		

Moreover, different levels of the aforementioned four types of faults are considered as well in this study. Specifically, eight cases of individual fault experiments are performed and studied on the small scale laboratory PV array, including two short-circuit faults (one module and two modules short-circuited, denoted as Short Circuit 1 and Short Circuit 2 respectively), string and array degradation faults (denoted as Degradation1 and Degradation2 respectively), and open-circuit fault of one PV string (denoted as Open Circuit), three partial shading (one

module, two modules and three modules in shading, denoted as Shading1, Shading2, and Shading3 respectively), as illustrated in Fig. 3(a). To simulate the faults and normal status of the PV array, a flexible fault simulation circuit is designed in the Simulink based model, which is illustrated in Fig. 3(b). The short-circuit faults are simulated by putting a resistor R_{sc} with very small resistance between the PV module terminals, while the open-circuit faults are simulated by adding a resistor R_{oc} with very large resistance in series with a PV string. String and array degradation faults are simulated by connecting a resistor R_{de} with small resistance in series with a PV string or PV array. Partial shading is simulated by adding a gain on the irradiance input of relevant PV modules. As summarized in Table 2, simulation of the normal status of PV array (PVA) and the eight cases of the PVA faults is implemented by assigning corresponding values to the parameters of the gains or resistors, including Gain_ps1, Gain_ps2, Gain_ps3, R_{sc1}, R_{sc2}, R_{de1}, R_{de2}, and R_{oc}. In addition, to illustrate the impact of different faults, the I-V and P-V characteristic curves of the simulated PV array of the nine cases are plotted together in Fig. 4(a) and (b), which are simulated under a typical ambient condition (irradiance: 800 W/m², temperature: 25 °C).

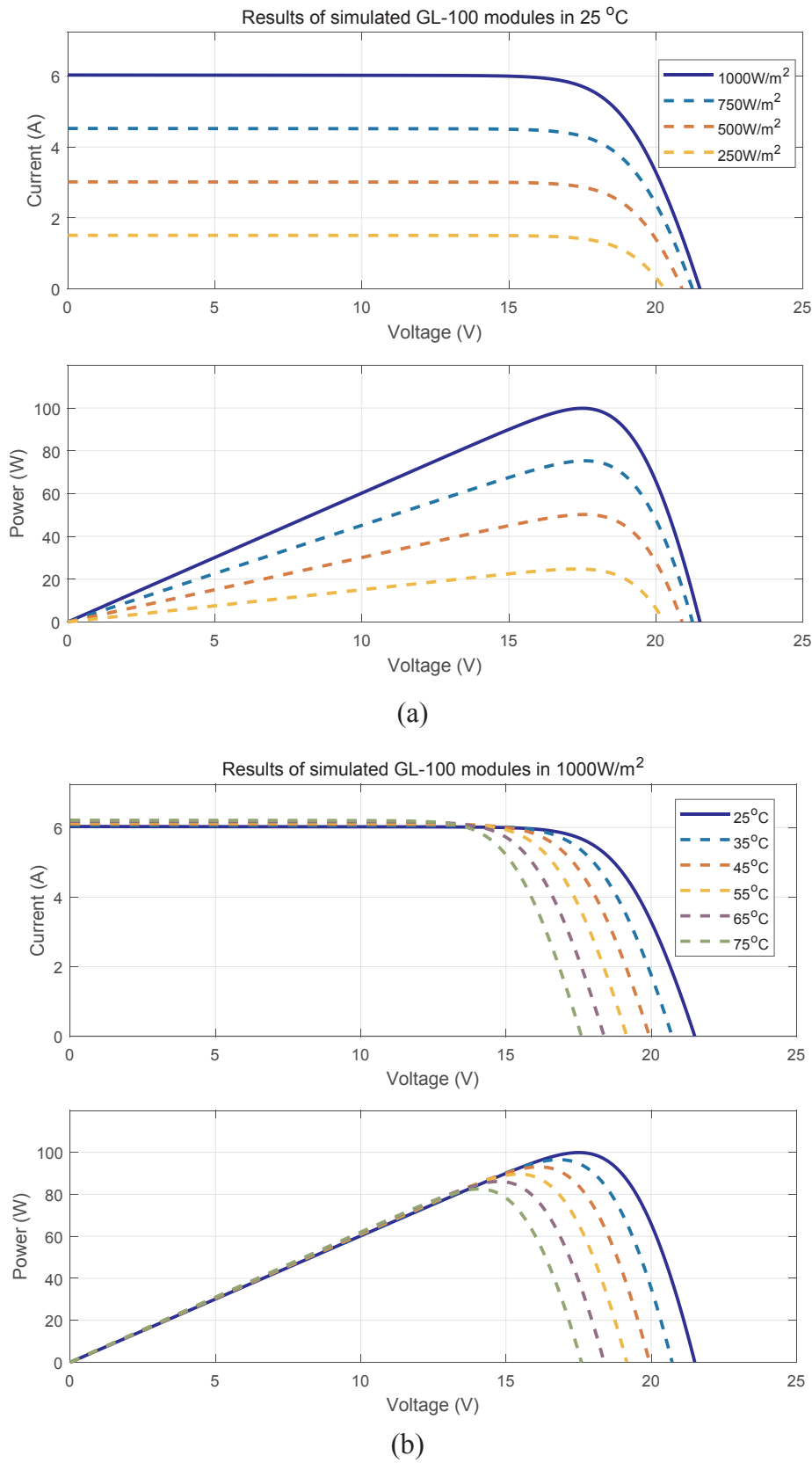


Fig. 2. Typical I-V and P-V curves of Simulink based model of PV module.

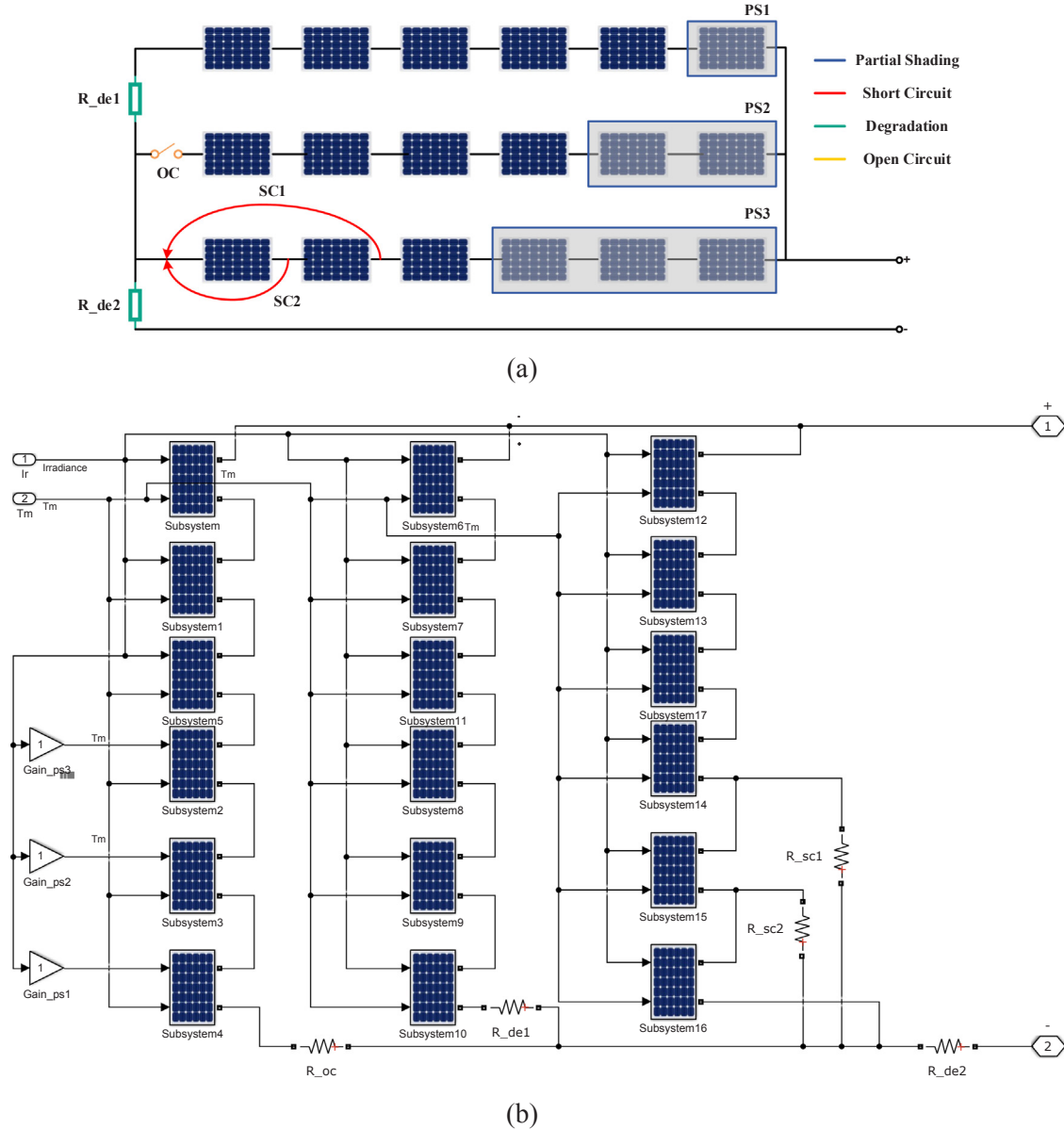


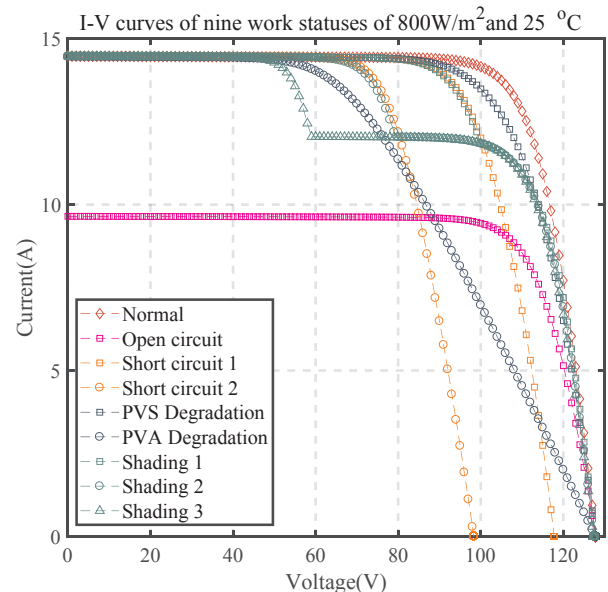
Fig. 3. (a) schematic diagram and (b) simulation circuit for the faults.

Table 2
Parameters values of the added components under different work statuses.

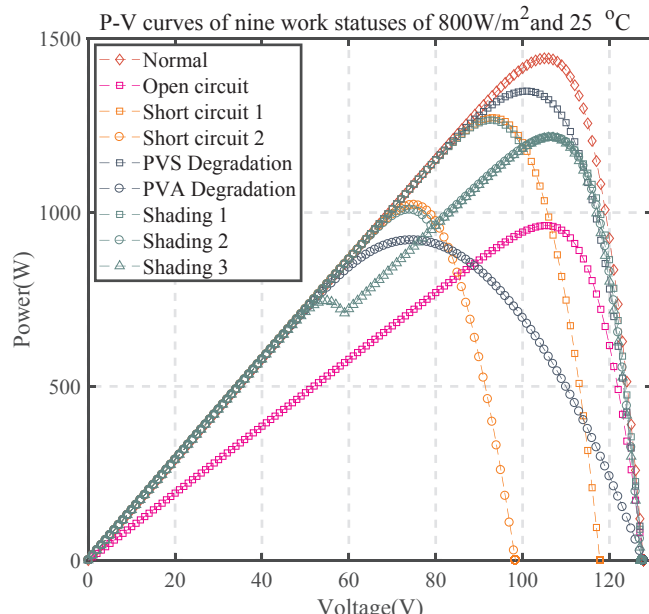
Parameters	Value in normal status	Value in faulty status
Gain_ps1	1	0.5
Gain_ps2	1	0.5
Gain_ps3	1	0.5
R_sc1 (Ω)	100,000	0.001
R_sc2(Ω)	100,000	0.001
R_de1(Ω)	0.001	3
R_de2(Ω)	0.001	3
R_oc (Ω)	0.001	100,000

As summarized in Table 2, the normal working status of the PV array are simulated by setting the gains (Gain_ps1, Gain_ps2 and Gain_ps3) to be 1, the resistances of series resistors (R_{de1} , R_{de2} and R_{oc}) to be nearly zero (0.001), the resistance of parallel resistors (R_{sc1} and R_{sc2}) to be a large value (100000). In this way, the additionally added components will have very little impact on the PV array, and the simulation can be run normally in Simulink environment.

For other eight cases of the faults simulation, some of the corresponding parameters are changed to appropriate values different from the normal ones. Specifically, there are three main partial shading cases with parameters set as follows: partial shading to PVM1 denoted as “Shading 1” (Gain_ps1: 0.5), partial shading to PVM1-2 denoted as “Shading 2” (Gain_ps1: 0.5, Gain_ps2: 0.5), partial shading to PVM1-3 denoted as “Shading 3” (Gain_ps1: 0.5, Gain_ps2: 0.5, Gain_ps3: 0.5), while other parameters are set to the normal ones. In the cases of the partial shading, it can be observed from Fig. 4 that the shapes of curves are obviously distorted and there are more than one local maximum power peaks in both IV and PV characteristic curves. The two short-circuit faults are configured and denoted as “Short circuit 1” (R_{sc1} : 0.001 Ω) and “Short circuit 2” (R_{sc2} : 0.001 Ω) respectively, while other parameters remain normal ones. As shown in Fig. 4, compared with the normal status, the open circuit voltage V_{oc} and maximum power point P_m of the PV array are obviously reduced by the short-circuit faults, but the short-circuit current basically remains the same. The PV string degradation fault denoted as “PVS degradation” and simulated by setting the R_{de1} to be 3 Ω , while the PV array degradation denoted as “PVA degradation” is simulated by setting R_{de2} to 3 Ω as well. It can be seen



(a)



(b)

Fig. 4. (a) I-V characteristic curves of the simulated PV array under different fault conditions; (b) P-V characteristic curves of the simulated PV array under different faults.

in Fig. 4 that the short-circuit current and open-circuit voltage keep unchanged in the cases of degradation, but the MPP point is lower than the normal one. In addition, power reduction of the PVA degradation is much more severe than the PVS degradation. The open-circuit fault denoted as “Open Circuit” is emulated by configuring the R_{oc} to be 100000. In case of the open-circuit fault, the open-circuit voltage remains unchanged, while the output current will significantly decrease. Accordingly, the maximum power point P_m can be obviously reduced. Therefore, as demonstrated in Fig. 4, different faults obviously have different impact on the output I-V curves, which can imply the potential feasibility of fault detection and classification directly based on I-V characteristic curves and ambient conditions.

3. Deep residual network based fault detection and diagnosis for photovoltaic arrays

In view of the high performance and automatic feature extraction capability of the deep learning techniques, the emerging powerful deep residual network (ResNet) is proposed for fault detection and diagnosis (FDD) of PV arrays directly using the output I-V characteristic curves and corresponding ambient conditions. Firstly, a large number of I-V curves of the PV array are acquired by I-V testers under various ambient conditions for each case of operating status (including the normal status and fault statuses), which contain much more information than the electrical data of dynamic operating points. Then, the raw I-V curves and ambient irradiance and temperature are preprocessed to build the dataset. Next, a new ResNet structure is proposed as the FDD model. Finally, the ResNet based FDD model is trained and tested based on the established dataset.

3.1. Data preprocessing

The preprocessing of raw I-V curves and corresponding ambient conditions is to provide high quality data for training and running the FDD model efficiently and effectively, which includes two steps. The first step is to down-sample the raw I-V curves. The second step is to combine the voltage and curve vectors of each I-V curve with its ambient condition to form a two-dimensional data sample as the input of the FDD model.

Original I-V curves obtained by most I-V testers consist of a large number of data points with non-uniform distribution. Especially, most data points remain in the range between the short-circuit point and the MPP, while there are much less data points between the MPP and open circuit point. To improve the quality and reduce the data size of the dataset for training the FDD model, the raw I-V curves are firstly resampled and down-sampled to provide new I-V curves with uniform distribution and smaller data size. Specifically, a current–voltage based bilinear interpolation methods is proposed to down-sample raw IV curves by Eq. (4) and Eq. (5), reducing the original 200 data points to 40 points for every I-V curve. The specific flowchart of the down-sampling is illustrated in Fig. 5. Firstly, 20 new data points are

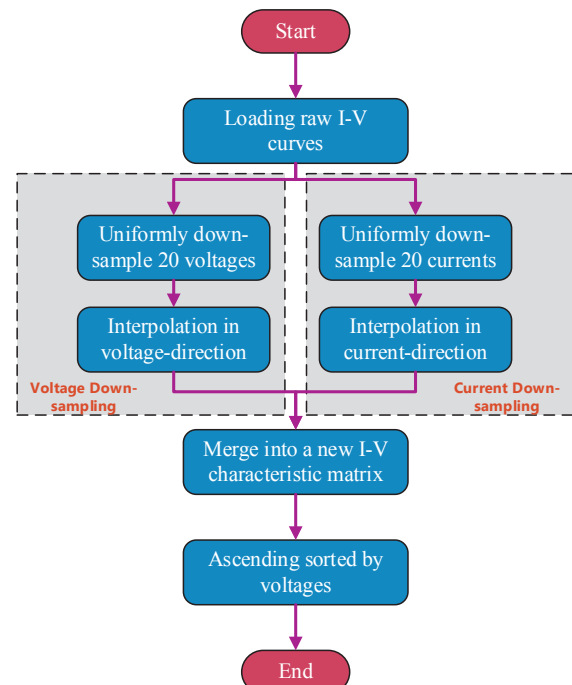


Fig. 5. Flowchart of the down-sampling process.

resampled from the raw I-V curve along the voltage axis and with uniformly-spaced voltage in the range of $[0, V_{oc}]$, while other 20 new data points are resampled along the current axis with uniformly-spaced current $[0, I_{sc}]$ respectively. Then, the unknown voltage or current of the new data points are obtained by the linear interpolation. Specifically, the voltages of the 20 new data points with equispaced currents are calculated by bilinear interpolation as given in Eq. (4), while the current of other 20 new data points with equispaced voltages are calculated by bilinear interpolation as given in Eq. (5). After obtaining both the voltage and current values, the 40 new resampled data points are merged and sorted in descending order of the voltage, so as to form a new I-V curve.

$$V_{Rx,n} = \frac{(I_{Rx} - I_1) \cdot V_2 + (I_2 - I_{Rx}) \cdot V_1}{I_2 - I_1} \quad (4)$$

$$I_{Rx,n} = \frac{(V_{Rx} - V_1) \cdot I_2 + (V_2 - V_{Rx}) \cdot I_1}{V_2 - V_1} \quad (5)$$

where the I_{Rx} and V_{Rx} represent the equispaced voltages and currents of the resampled data points respectively, while $I_{Rx,n}$ and $V_{Rx,n}$ are corresponding interpolated currents and voltages to the equispaced voltages (V_{Rx}) and currents (I_{Rx}). In addition, V_1 , V_2 , I_1 and I_2 are the values of voltages and currents of the left-side and right-side data points of the raw I-V curves, which are the closest to the resampled data points.

The magnitude of the output I-V characteristic curves of a PV array highly depends on the input ambient conditions. Therefore, the irradiance and temperature should be included into the data sample, so as to eliminate the impact of different ambient conditions on the dataset. In view of that the convolutional neural networks feature powerful automatic feature extraction on two dimensional data (such as images), the I-V curves and ambient conditions are formed to be two dimensional, as shown in Fig. 6. Firstly, the irradiance and temperature are repeated to form a column vector of the same length of the I-V curves respectively. Then, the temperature vector, irradiance vector and I-V curve matrix are concatenated to eventually form the feature of a data sample of two-dimensional 40×4 matrix, as illustrated in Fig. 6. In addition, one-hot encoding method is used the label the data samples.

Specifically, the one-hot codes ([1, 0, 0, 0, 0, 0, 0, 0, 0], [0, 1, 0, 0, 0, 0, 0, 0, 0], ..., [0, 0, 0, 0, 0, 0, 0, 0, 1]) are used to label the nine different operating conditions in this study, including the Normal, Shading1, Shading2, Shading3, Degradation1, Degradation2, Short Circuit1, Short Circuit2 and Open Circuit (as detailed in subsection 2.2).

Finally, all data samples are randomly divided into three subsets, including training set, hold-out validation set and test set. The proposed model is established using the training dataset and then further improved using hold-out validation set, while the unknown data samples in test dataset are used to test the trained model in terms of accuracy and generalization performance.

3.2. Deep residual network based fault detection and diagnosis model

In contrast to traditional machine learning approaches, such as back-propagation neural network (BPNN), support vector machine (SVM), extreme learning machine (ELM) etc., deep learning techniques generally have better accuracy and generalization performance. Especially, most deep learning techniques are capable of automatic non-linear feature extraction. As one of the most popular deep neural network structures in the field of deep learning, deep residual network (ResNet) was firstly proposed by He et al. [62] in 2015 for image recognition, which is widely used in various pattern recognition tasks now. Compared to other deep learning methods, such as plain CNN, the advantage of the ResNet includes a higher training speed, easier gradient transmission and deeper neural network with less gradient vanishing or explosion, and so on. Especially, based on the ResNet structure, deeper networks can be exploited to achieve a higher performance for both regression and classification tasks. Therefore, in this paper, the ResNet is explored as a multi-classifier to detect and diagnose the normal status and different faults of a PV array. The architecture of the original ResNet of 34-layers is proposed for the complex image classification as detailed in Table 3, which is composed of 2-dimensional convolution layers, pooling layers and fully-connected layers. However, it is too complicated for the PV array diagnosis problem with much less features, which causes the low computation efficiency and even overfitting problem. Therefore, a simplified ResNet is proposed in this paper

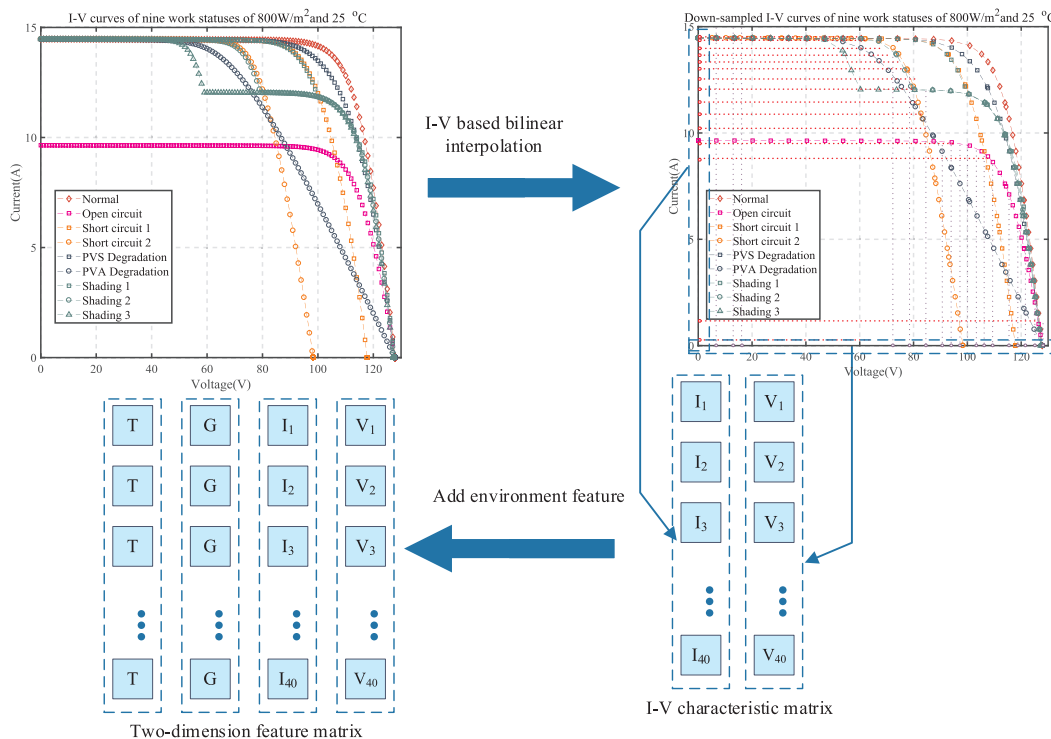


Fig. 6. Illustration of the data preprocessing.

Table 3
Detailed configuration of the original 34-layers ResNet.

Layer name	Output dimension	Detailed architecture for the proposed ResNet
Conv2D	$112 \times 112 \times 64$	$k = 4 \times 4, C_{out} = 2$
Conv2D	$56 \times 56 \times 64$	MaxPool, $k = 3 \times 3$
		$\begin{bmatrix} k = 3 \times 3, C_{out} = 64 \\ k = 3 \times 3, C_{out} = 64 \end{bmatrix} \times 3$
Conv2D	$28 \times 28 \times 128$	$\begin{bmatrix} k = 3 \times 3, C_{out} = 128 \\ k = 3 \times 3, C_{out} = 128 \end{bmatrix} \times 4$
Conv2D	$14 \times 14 \times 256$	$\begin{bmatrix} k = 3 \times 3, C_{out} = 256 \\ k = 3 \times 3, C_{out} = 256 \end{bmatrix} \times 6$
Conv2D	$7 \times 7 \times 512$	$\begin{bmatrix} k = 3 \times 3, C_{out} = 512 \\ k = 3 \times 3, C_{out} = 512 \end{bmatrix} \times 3$
Linear Classification	1×1	AvgPool 1000-d FC

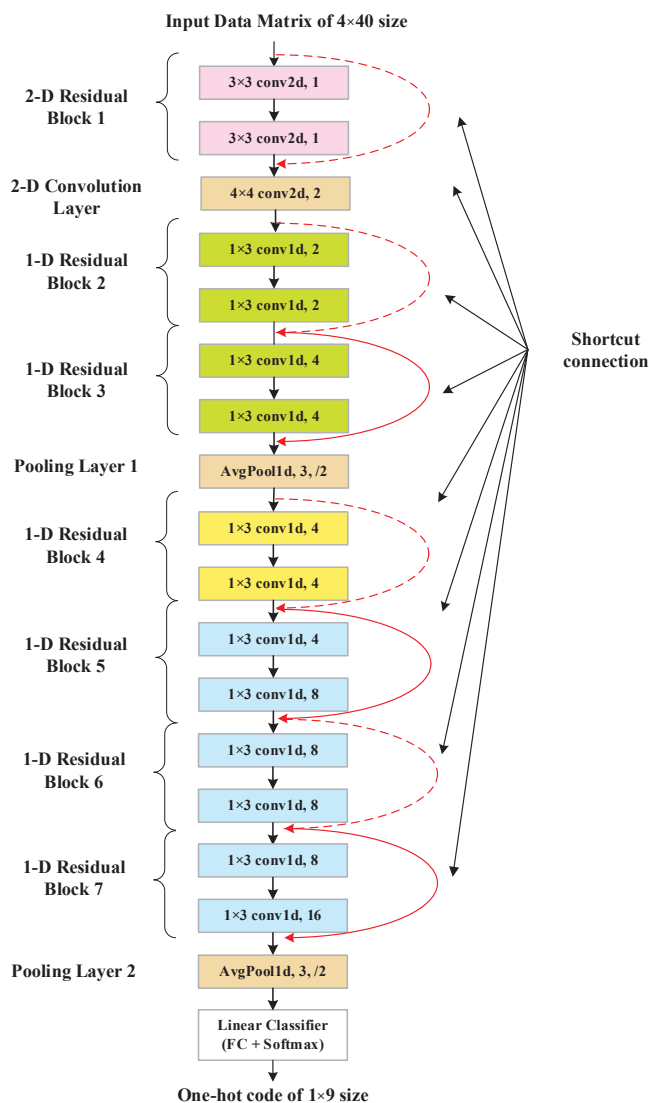


Fig. 7. Architecture for the proposed simplified ResNet model.

for PV fault diagnosis.

Considering the aforementioned advantages of the ResNet, a new simplified structure of the ResNet network is proposed as the FDD model for PV arrays. As illustrated in Fig. 7, the proposed ResNet structure consists of different layers, including (1) Residual blocks: referring to two convolution layers with one shortcut connection; (2)

Input: the mini-batch data $X_n \times m = \{x_1, x_2, \dots, x_m\}$

Output: $Y = \{y_i = \text{BatchNorm}_{\gamma, \beta}(x_i)\}, i = 1, 2, \dots, m$

$$\mu_\beta = \frac{1}{M} \sum_{i=1}^M x_i$$

$$\sigma_\beta^2 = \frac{1}{M} \sum_{i=1}^M (x_i - \mu_\beta)^2$$

$$\hat{x}_i = \frac{x_i - \mu_\beta}{\sqrt{\sigma_\beta^2 + \epsilon}}$$

$$y_i = \gamma \hat{x}_i + \beta \equiv \text{BatchNorm}(x_i)$$

Fig. 8. Specific process of the batch normalization transform.

Convolutional layers (Conv): automatically extracting effective features from the input feature maps by a set of small receptive fields (or kernel) with enough depth; (3) Average pooling layers (AvgPool): down-sampling the feature matrix by dividing the input into rectangular regions and computing the average of each region; (4) Linear classifier: achieving the classification by linear decision. These different layers in the proposed ResNet are detailed as follows.

(1) Convolutional Layer: As a popular deep learning structure, the standard two-dimensional convolutional layer (Conv2d) can greatly decrease the free parameters in training process and promote the performance thanks to the advantages of the local receptive field and weight sharing. Compared with the fully connected layer, the Conv2d processes the inputs using a series of filter (called kernel in this paper) in a small region (respective field) with locally connections. Essentially, the calculation process in convolution layer is a mathematical operation to slide each filter on the input matrix and compute the dot product on the kernel and input at all position, which has the same principle as one-dimensional convolution (Conv1d). The specific computation process of the Conv2d is defined in Eq. (6), while the Conv1d is defined by cross-correlation operator as Eq. (7).

$$\text{Conv2d}(x) = \sum_{w=0}^{m-1} \sum_{h=0}^{m-1} K_{w,h} \cdot x_{(i+w),(j+h)} \quad (6)$$

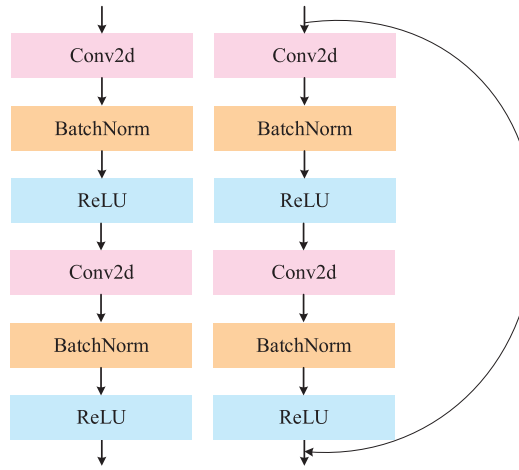
$$\text{Conv1d}(x) = \sum_{k=0}^{C_{in}-1} K_k * x \quad (7)$$

where the x is the 2-D output from the previous layer and i, j are used to record the coordinates in a 2-D input. In addition, the K represents the $m \times m$ kernel matrix, which is a learnable parameter in the training process. The w and h are the position index in the 2-D kernel matrix. In Eq. (7), K_k is the kernel size for k_{th} input neuron and $*$ is the cross-correlation operator without zero padding.

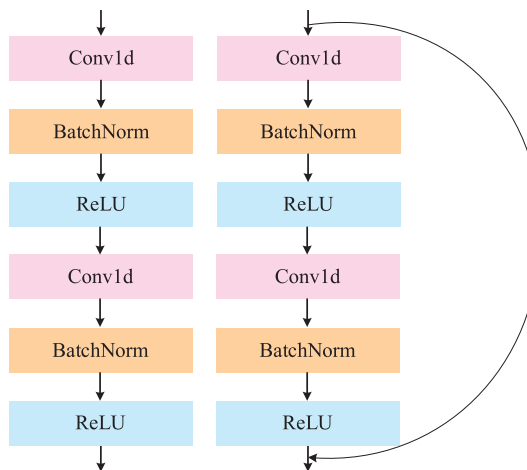
(2) Pooling layer: The pooling layer, usually inserted into successive convolution layers, is primarily used to reduce spatial size of the feature map and effectively control overfitting as Eq. (8) and (9). Specifically, the dimension computation is the same as the Conv1d and Conv2d. In this paper, the average pooling (AvgPool) is chosen to operate on each depth and slice of feature map independently, which replaces the entire receptive field by averaging.

$$w_{out} = \frac{w_{in} - k_w}{s} + 1 \quad (8)$$

$$h_{out} = \frac{h_{in} - k_h}{s} + 1 \quad (9)$$



(a) Architecture of the 2-D plain convolution block (left) and the 2-D residual block (right)



(b) Architecture of the 1-D plain convolution block (left) and the 1-D residual block (right)

Fig. 9. Internal structure of the residual blocks.

where the w_{in} and h_{in} represent the width and height of the input two-dimensional matrix, while the w_{out} and h_{out} are those of the output. In addition, k_w and k_h are the width and height for kernel size.

(3) Activation function: To learn complicated and non-linear features from the raw dataset, the nonlinear activation function is used to increase the nonlinearity of the extracted features. In this paper, the nonlinear activation function Rectified Linear Unit (ReLU) is selected, as defined Eq. (10) where the x is the input feature, which can greatly accelerate the convergence and alleviate the vanishing gradient issue. In addition, the simple activation function without limitation is much more computation efficient, in comparison to the Sigmoid with the exponential operation.

$$\text{ReLU}(x) = \begin{cases} 0, & x < 0 \\ x, & x \geq 0 \end{cases} \quad (10)$$

(4) Batch normalization: Deep learning techniques usually participate the training set into many small sets called mini-batches and then train the model based on the mini-batches, which can achieve a good tradeoff between the convergence and computation complexity. However, mini-batch method tends to suffer internal covariate shift that may decrease the training speed and stability. Batch normalization (BatchNorm) is proposed by Ioffe and Szegedy to reduce the internal covariate shift by normalizing the input layers through scaling and adjusting the activations [69], thus improving

the training speed and reliability while alleviating the overfitting and gradient vanishing/explosion issues with a higher learning rate. The BatchNorm transform is detailed in Fig. 8, where the input x consists of m mini-batch samples and n represent the dimension of every sample x_i . In addition, μ_β and σ_β are the mean and variance of the mini-batch samples respectively. There are two learnable parameters γ and β in Fig. 8. The default value of the last constant coefficient ϵ is 0.0001, which is a very small value to avoid a zero denominator.

(5) Residual Blocks: The inner structure of the residual block is shown in Fig. 9. Compared to a plain CNN, there is a shortcut connection from input to output in a residual block. With the shortcut (solid line in Fig. 7), the inputs can be attached to the output directly as given in Eq. (11), when the input and output are of the same dimension. When the dimension is different (dotted line in Fig. 7), a dimension matching factor is introduced to match the input and output dimensions as given in Eq. (12).

$$y = F(x) + x \quad (11)$$

$$y = F(x) + W_x x \quad (12)$$

where the x and y are the input and output of residual blocks, the function F represents the mapping relationship from inputs to outputs and the W_x is the dimension matching factor.

In Fig. 9(a), the 2-D residual block is mainly composed of 2-D convolution layer (Conv2d), batch normalization layer (BatchNorm)

Table 4

Specific configuration for the proposed ResNet structure.

Layers	Output dimension	Detailed structure of the proposed ResNet
Input Layer	$40 \times 4 \times 1$	
2-D Residual Block 1	$40 \times 4 \times 1$	$k = 3 \times 3, C_{out} = 1, ss = 2, p = 1$ $\begin{bmatrix} k = 3 \times 3, C_{out} = 1, ss = 1, p = 1 \\ k = 3 \times 3, C_{out} = 1, ss = 1, p = 1 \end{bmatrix}$
2-D Conv	$37 \times 1 \times 2$	$k = 4 \times 4, C_{out} = 2, ss = 1, p = 0$
Dimension Squeeze	37×2	
1-D Residual Block 1	37×2	$\begin{bmatrix} k = 3, C_{out} = 2, ss = 1, p = 1 \\ k = 3, C_{out} = 2, ss = 1, p = 1 \end{bmatrix}$
1-D Residual Block 2	37×4	$\begin{bmatrix} k = 3, C_{out} = 4, ss = 1, p = 1 \\ k = 3, C_{out} = 4, ss = 1, p = 1 \end{bmatrix}$
AvgPool 1	18×4	$k = 3, C_{out} = 4, ss = 2, p = 0$
1-D Residual Block 3	18×4	$\begin{bmatrix} k = 3, C_{out} = 4, ss = 1, p = 1 \\ k = 3, C_{out} = 4, ss = 1, p = 1 \end{bmatrix}$
1-D Residual Block 4	8×8	$\begin{bmatrix} k = 4, C_{out} = 8, ss = 2, p = 0 \\ k = 3, C_{out} = 8, ss = 1, p = 1 \end{bmatrix}$
1-D Residual Block 5	8×8	$\begin{bmatrix} k = 3, C_{out} = 8, ss = 1, p = 1 \\ k = 3, C_{out} = 8, ss = 1, p = 1 \end{bmatrix}$
1-D Residual Block 6	8×16	$\begin{bmatrix} k = 3, C_{out} = 16, ss = 1, p = 1 \\ k = 3, C_{out} = 16, ss = 1, p = 1 \end{bmatrix}$
AvgPool 2	3×16	$k = 4, C_{out} = 16, ss = 2, p = 0$
Linear Classifier	9	FC layer and Softmax output

and activation function ReLU, while the 1-D residual block only changes the 2-D convolution layer to 1-D convolution layer (Conv1d) as illustrated in Fig. 9(b).

Table 5

Detailed configuration of the compared CNN structure.

Layer name	Output dimension	Detailed architecture for the proposed ResNet
Input Layer	$40 \times 4 \times 1$	
2-D CNN	$37 \times 1 \times 1$	$k = 4 \times 4, C_{out} = 1, ss = 1, p = 0$
Dimension Squeeze	37×1	
1-D CNN	18×3	$k = 3, C_{out} = 3, ss = 2, p = 0$
1-D CNN	18×5	$k = 3, C_{out} = 5, ss = 1, p = 1$
MaxPool1D	8×5	$k = 4, ss = 2$
1-D CNN	8×8	$k = 3, C_{out} = 8, ss = 1, p = 1$
MaxPool1D	4×8	$k = 2, ss = 2$
1-D CNN	4×16	$k = 3, C_{out} = 16, ss = 1, p = 1$
MaxPool1D	1×16	$k = 4, ss = 1$
FC	10	Fully-connected Layer
Linear Classifier	10×9	FC layer and Softmax output

(6) Linear Classifier: After the feature extraction and compression by the convolution layers, the linear classifier is used to compute the classification results. In this paper, the linear classifier is composed of a fully connected (FC) layer and a Softmax function. Specifically, the FC layer connects every neuron from one layer to another, which has the same principle as multi-layer perceptron. The computation of the FC layer using dot product is shown in Eq. (13). However, the output of the FC is a continuous value that cannot directly represent the discrete classification results. To implement classification, as defined in Eq. (14), the Softmax function is used to normalize the input vector into a vector of the probability belonging to each class, and the class with the maximum probability is chosen as the final prediction output.

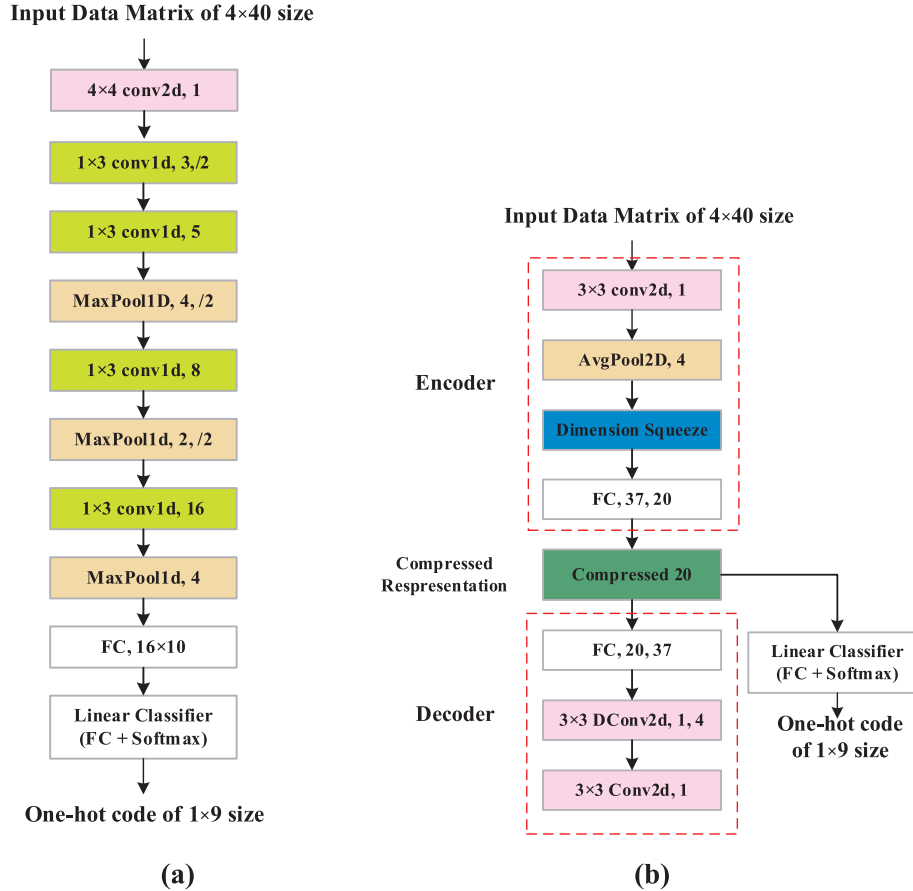
**Fig. 10.** The detailed architecture of the CNN (a) and the CAE (b) networks for comparison.

Table 6

Detailed configuration of the compared CAE structure.

Layer name	Output dimension	Detailed architecture for the proposed ResNet
Input Layer	$40 \times 4 \times 1$	
2-D CNN	$40 \times 4 \times 1$	$k = 3 \times 3, C_{out} = 1, ss = 1, p = 1$
AvgPool2D	$37 \times 1 \times 1$	$k = 4 \times 4, C_{out} = 1, ss = 1, p = 0$
Dimension Squeeze	37	
FC Layer	20	Fully-connected Layer
Compressed represent	20	Compressed features acquired from Encoder
FC layer	37	$k = 4, ss = 2$
Dimension Unsqueeze	$37 \times 1 \times 1$	
1-D DCNN	$40 \times 4 \times 1$	$k = 4, C_{out} = 1, ss = 1, p = 0$
1-D CNN	$40 \times 4 \times 1$	$k = 3, C_{out} = 1, ss = 1, p = 1$
1-D CNN	4×16	$k = 3, C_{out} = 16, ss = 1, p = 1$
Linear Classifier	9	FC layer and Softmax output

$$y = W_{N \times D}x_{D \times M} + b_{N \times M} \quad (13)$$

$$\text{Softmax}(x_i) = \frac{e^{x_i}}{\sum_{k=1}^{C_o} e^{x_k}}, i = 1, 2, \dots, C_o \quad (14)$$

where the $W_{N \times D}$ is the weight matrix of $N \times D$ dimension and $x_{D \times M}$ is input feature map of $D \times M$ dimension, while the b is bias. In Eq. (14), the x_i is one of the elements in the output layer and C_o is the dimension of the output (9 in this paper).

Specifically, the proposed ResNet structure is illustrated in Fig. 7. The input layer of the ResNet is a data matrix of 4×40 size, while the output is one-hot code of 1×9 size. The first 2-D residual block is used for feature extraction from the input data without manual intervention and the following 2-D convolution layer is used for feature compression for higher training speed and lower computation complexity. After the feature extraction modules, there are six 1-D residual blocks with an AvgPool added between the second and third 1-D residual blocks for further feature compression. Another AvgPool is added for matching the dimension before the linear classifier. Finally, a linear classifier (Linear) is used for classification, which consists of a FC layer and Softmax output layer. Inspired by the original ResNet paper, the residual blocks except 1-D residual block are set to adjust the output channels, while the first single 2-D convolution layer and pooling layer are used to configure the dimension of the output. In addition, the kernel size of the 1-D residual blocks is set to 4 for lower algorithm complexity and better dimension matching. The specific configuration for the proposed ResNet structure is listed in Table 4.

Compared with the original ResNet firstly proposed in [62], the architecture of the proposed ResNet structure is firstly simplified from

Step 1. Set the initial value for $lr, \beta_1, \beta_2, \epsilon, Epoch$;
Step 2. Randomly select optimization parameter θ and set $m = 0, v = 0, epoch = 0$;
Step 3. Update the parameters when $epoch < Epoch$:
Step 3.1. Increase counters $epoch += 1$;
Step 3.2. Calculate $g = \frac{1}{n} \nabla_{\theta} \sum_{i=1}^n J(f(x^{(i)}; \theta), y^{(i)})$;
Step 3.2. Calculate $m_{epoch} = \beta_1 \cdot m_{epoch-1} + (1 - \beta_1) \cdot g_{epoch}$;
Step 3.3. Calculate $v_{epoch} = \beta_2 \cdot v_{epoch-1} + (1 - \beta_2) \cdot g_{epoch}^2$;
Step 3.4. Calculate $\hat{m}_{epoch} = \frac{m_{epoch}}{1 - \beta_1^{epoch}}$ and $\hat{v}_{epoch} = \frac{v}{1 - \beta_2^{epoch}}$;
Step 3.5. Update parameters θ : $\theta_{epoch+1} = \theta_{epoch} - lr \frac{\hat{m}_{epoch}}{\sqrt{\hat{v}_{epoch} + \epsilon}}$;
Step 4. Return the optimal solution θ ;

Fig. 11. Pseudo-code of the Adam optimization algorithm.**Table 7**

Setting of hyper-parameters in training process.

Hyper-parameters	Value
n	512
lr	1e-3
β_1	0.995
β_2	0.999
Epoch	500
ϵ	1e-8

34 layers to 18 layers with the guaranteed precision, which greatly improved the efficiency of PV array FDD. Secondly, the feature map is decimated to be a scalar by the Conv2d operation, and the Conv1d operation is further used to reduce the training features for higher efficiency. Moreover, the introduced Conv1d has better feature extraction ability than the fully-connected Layer.

For further evaluating the superiority of the proposed ResNet based fault diagnosis, two others commonly used deep learning structures are used for comparison, including fully connected convolution neural network (CNN) and convolutional auto-encoder (CAE). The specific architectures of the CNN and CAE are detailed in Fig. 10(a) and (b). In addition, the configuration for CNN and CAE is listed in Tables 5 and 6. Specifically, inspired by the AlexNet and VGG networks for image recognition [70,71], the CNN for comparison is composed of Conv2d, Pooling layer and fully connected layers. In this paper, some Conv2d is replaced by Conv1d to ensure the features dimension matching and automatic features extraction as Fig. 10(a). In terms of the CAE, the Deconvolution (DCONV) as the inverse convolution operation is used to generate the original features, and the optimal features are determined by calculating the differences between original feature and generating features. Finally, the optimal compressed presentation is used for classification, which is marked in green in Fig. 10(b).

3.3. Training of the fault detection and diagnosis model

After determining the neural network structure, the ResNet network need to be trained using the labelled dataset to obtain the internal weights and biases. Once the network is trained, the ResNet based model can be used to perform fault detection and diagnosis for unlabeled data. As a kind of supervised learning methods, the training of the ResNet model is to minimize the loss function on the labelled training set by learning algorithms. The loss function to be minimized in this paper is defined as the hold-out entropy as given in Eq. (15).

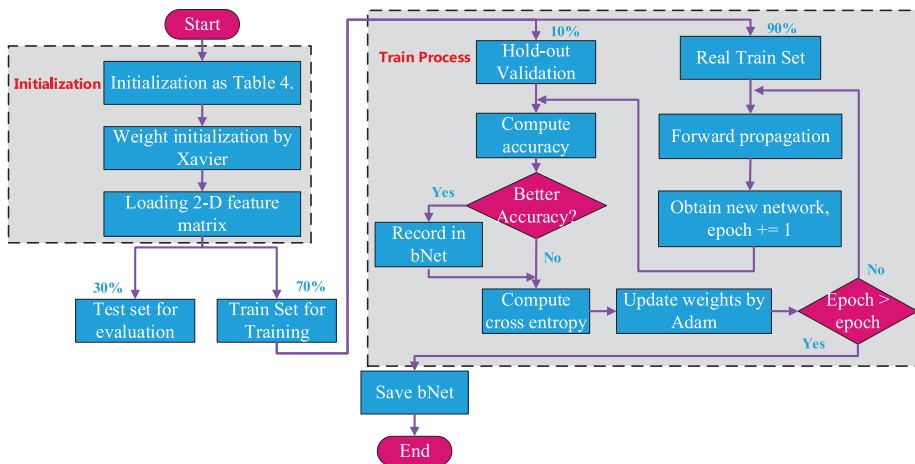


Fig. 12. Flowchart for the training process of the deep learning based FDD model.

Table 8
Distribution of the simulated data samples.

Fault Types	Type Number	Number of samples		
		Training set	Cross Validation	Testing set
Normal	1	1872	220	893
Shading 1	2	1872	220	891
Shading 2	3	1876	220	893
Shading 3	4	1873	220	893
Degradation 1	5	1874	219	893
Degradation 2	6	1878	221	893
Short Circuit 1	7	1872	219	893
Short Circuit 2	8	1871	220	892
Open Circuit	9	846	99	404
Totally		15,834	1858	7545

$$J(w) = \frac{1}{N} \sum_{n=1}^N [y_n \log \hat{y}_n + (1 - y_n) \log(1 - \hat{y}_n)] \quad (15)$$

where N is the classification number of all the data samples, which is equal to 9 in this paper. The y_n is the one-hot real label of a data sample, while the \hat{y}_n is the probability vector of the prediction.

In this paper, the adaptive moment estimation (Adam) [72] is used to train the proposed ResNet, which is an adaptive learning rates algorithm and is superior especially in terms of the training speed. The Adam learning algorithm use an adaptive learning rate strategy to find the appropriate learning rate for each parameter in the training process. Specifically, the Adam keeps an exponentially decaying and an adaptive gradient by the first estimations and the second moment estimate. In addition, this algorithm is designed to use mini-batches of training dataset in every iteration to reach a good tradeoff between convergence and computation complexity. The Adam algorithm pseudo-code is

detailed in Fig. 11.

where the lr is the initial learning rate and ϵ is a very small constant. The β_1, β_2 are the average moving coefficients, whose default value are 0.9 and 0.999 respectively. The Epoch and epoch are the numbers of the total iteration and the current iteration respectively. In addition, the m and v are the first and second moment estimation. The g represents the gradient of the loss function J and n is the current mini-batch size. The θ represents the weights and biases in the proposed ResNet, which need to be optimized. The $f(\cdot)$ is the mapping relationship from the inputs to outputs. The specific the hyper-parameters are set as listed in the Table 7.

Moreover, gradient-based optimization algorithms are commonly influenced by the initial value θ , and the inappropriate initial values tend to cause the slow convergence and be trapped into the local optimal. To improve the quality of the initial point, the initialization technology Xavier [73], which determines the scale of the initialization by the numbers of the input and output neurons, is used to remain the same variance from the input and output for avoiding the gradient vanishing and explosion. In summary, the specific flowchart to train the ResNet based PV array FDD model can be illustrated in Fig. 12.

4. Simulation and real experiment studies

Based on a laboratory small-scale PV array and its Simulink based simulation model detailed in subsection 2.1, both of simulation and real fault experiments are performed to obtain simulated and actual datasets for validation of the proposed ResNet based fault detection and diagnosis (FDD) method. Specifically, as described in subsection 2.2, there are four types and eight cases of faults studied in this paper, including partial shading (Shading1, Shading 2 and Shading 3), PVS degradation (Degradation1), PVA degradation (Degradation 2), short circuit (Short-Circuit 1 and Short-Circuit 2) and Open Circuit. Firstly, the faults

Table 9
Comparison of classification accuracy of three models on the simulated data samples.

Item	CNN		CAE		ResNet	
	Training Accuracy (%)	Testing Accuracy (%)	Training Accuracy (%)	Testing Accuracy (%)	Training Accuracy (%)	Testing Accuracy (%)
Normal	99.95	100.0	99.95	99.89	100.0	100.0
Shading 1	100.0	99.66	99.84	99.44	100.0	100.0
Shading 2	100.0	100.0	100.0	100.0	100.0	100.0
Shading 3	92.37	92.39	96.85	97.65	100.0	100.0
Degradation 1	96.58	96.08	87.46	86.00	100.0	99.78
Degradation 2	99.95	99.89	98.88	99.22	100.0	100.0
Short Circuit 1	100.0	100.0	100.0	100.0	100.0	100.0
Short Circuit 2	100.0	100.0	100.0	100.0	100.0	100.0
Open Circuit	91.84	92.08	59.57	61.39	100.0	100.0

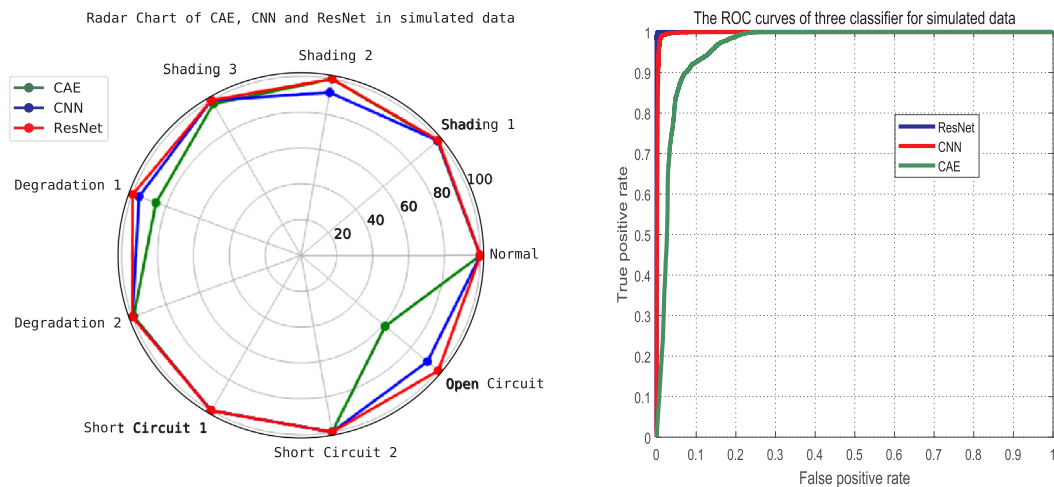


Fig. 13. Accuracy radar chart and ROC curves of the three models on simulation dataset.

Confusion Matrix										
Output Class	1	2	3	4	5	6	7	8	9	
	893 11.8%	0 0.0%	0 0.0%	0 0.0%	0 0.0%	0 0.0%	0 0.0%	0 0.0%	0 0.0%	100% 0.0%
	0 0.0%	891 11.8%	0 0.0%	0 0.0%	0 0.0%	0 0.0%	0 0.0%	0 0.0%	0 0.0%	100% 0.0%
	0 0.0%	0 0.0%	893 11.8%	0 0.0%	0 0.0%	0 0.0%	0 0.0%	0 0.0%	0 0.0%	100% 0.0%
	0 0.0%	0 0.0%	0 0.0%	893 11.8%	2 0.0%	0 0.0%	0 0.0%	0 0.0%	0 0.0%	99.8% 0.2%
	0 0.0%	0 0.0%	0 0.0%	0 0.0%	891 11.8%	0 0.0%	0 0.0%	0 0.0%	0 0.0%	100% 0.0%
	0 0.0%	0 0.0%	0 0.0%	0 0.0%	0 0.0%	893 11.8%	0 0.0%	0 0.0%	0 0.0%	100% 0.0%
	0 0.0%	0 0.0%	0 0.0%	0 0.0%	0 0.0%	0 0.0%	893 11.8%	0 0.0%	0 0.0%	100% 0.0%
	0 0.0%	0 0.0%	0 0.0%	0 0.0%	0 0.0%	0 0.0%	0 0.0%	892 11.8%	0 0.0%	100% 0.0%
	0 0.0%	0 0.0%	0 0.0%	0 0.0%	0 0.0%	0 0.0%	0 0.0%	0 0.0%	404 5.4%	100% 0.0%
		100% 0.0%	100% 0.0%	100% 0.0%	100% 0.2%	99.8% 0.0%	100% 0.0%	100% 0.0%	100% 0.0%	100% 0.0%

Fig. 14. The confusion matrix of the ResNet on the simulated dataset.

Table 10
Statistical comparison of average classification accuracy on the simulated dataset.

Algorithm	Accuracy (%)	Statistical analysis in 20 random runs			
		Max	Min	Mean	Std
CAE	Training set	98.333	83.870	94.257	0.042
	Testing set	98.092	93.314	94.395	0.044
CNN	Training set	99.943	99.009	99.696	0.003
	Testing set	99.960	98.529	99.672	0.004
ResNet	Training set	100.00	99.735	99.955	0.001
	Testing set	100.00	99.642	99.940	0.001

experiments are carried on the PV array under various ambient conditions to obtain raw I-V curves data by a I-V tester. Secondly, the raw I-V curves data together with the ambient conditions are preprocessed to build the dataset, as detailed in subsection 3.2. Finally, based on the simulated and real datasets, the proposed ResNet based FDD model are trained, tested and compared with other two deep learning algorithms

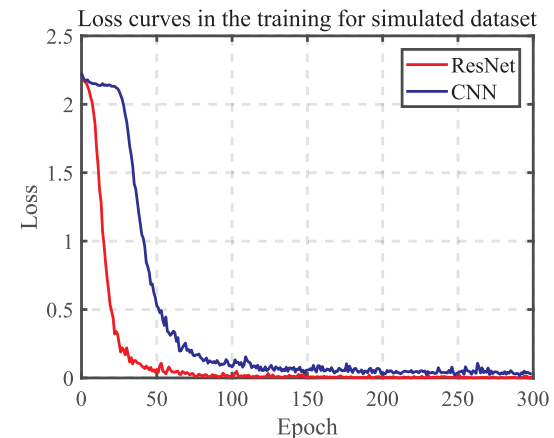


Fig. 15. Comparison of loss curves of the ResNet and CNN models on simulation dataset.

based FDD models, and then the results are discussed.

Additionally, in this study, the proposed ResNet model is realized using the Pytorch toolkit and Python script, and the deep learning algorithms are run in Pycharm environment on a desktop computer with the configuration: Intel (R) Core (TM) i5-4430S CPU @ 2.7 GHz, 16 GB (RAM), 2G GTX750Ti (GPU), and 64bits Ubuntu 16.04 operation system.

4.1. Simulation experiments and result analysis

Before conducting real fault experiments on the laboratory PV array, simulation fault experiments are carried out to verify the proposed ResNet based FDD model, as detailed in subsection 2.2. To make the FDD model more general for different ambient conditions, fault experiments are performed under a large range of different irradiance and temperature to acquire corresponding data samples. Specifically, the irradiance is controlled to range from 50 W/m^2 to 1000 W/m^2 with a small step of 10 W/m^2 , and the temperature is configured to vary from 10°C to 70°C with a small step of 2°C . Therefore, there are 2976 data samples for every case of faults as well as the normal status, and thus there are totally 26,784 data samples in the whole dataset. After easily excluding some abnormal data samples caused by the simulation environment, the number of the effective simulated data samples is 25237, and the detailed number of the data samples for each status is given in Table 8.

In order to train and evaluate the proposed ResNet based FDD

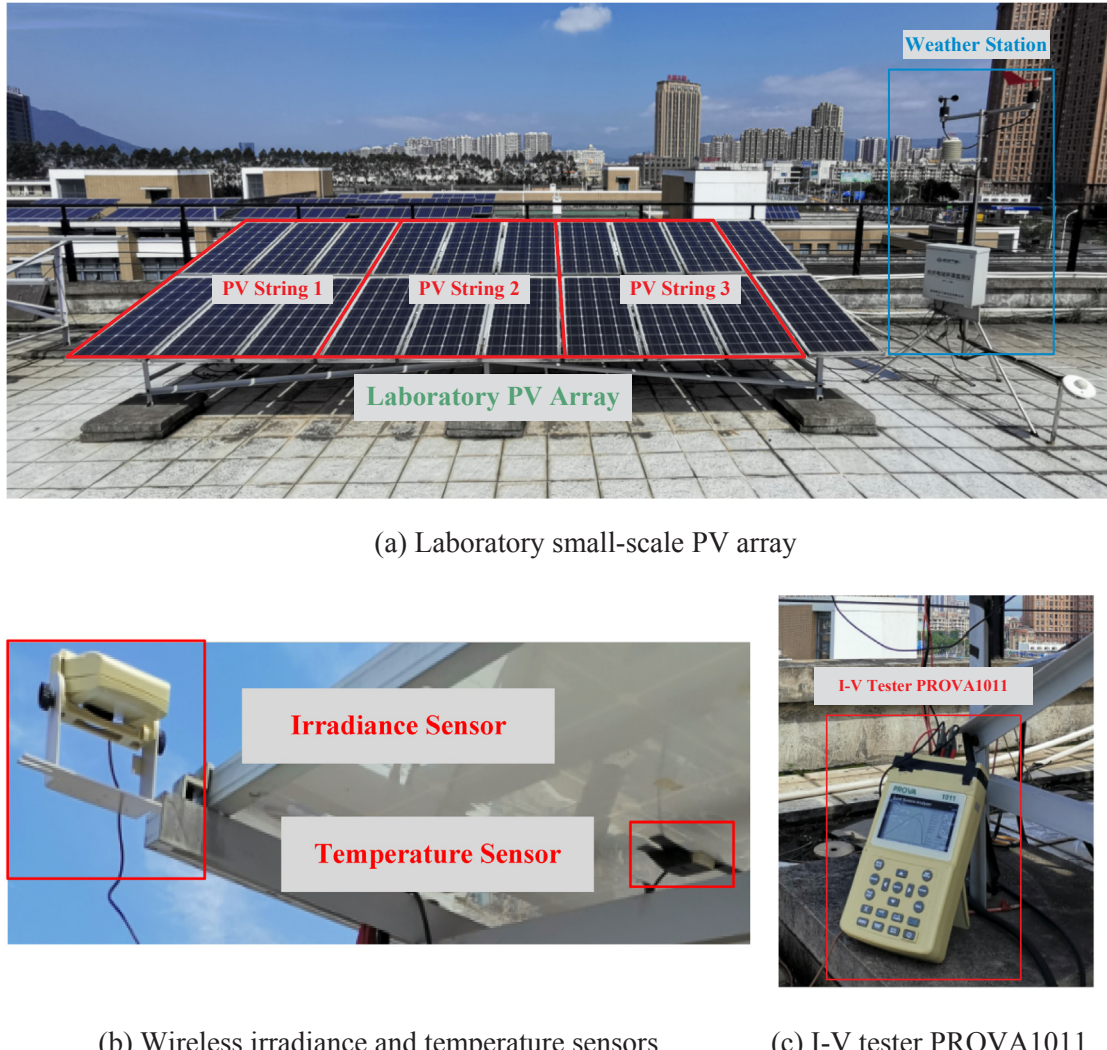


Fig. 16. The laboratory PV array and the PROVA1011 I-V tester.

model, the data samples of the same type in the dataset are randomly divided into three subsets, including training set with 70% of the data samples, hold-out validation set with 10% of the training set, and testing set with the remaining 30% data samples. The number of the data samples for the three subsets are summarized in Table 8. Both of training set and hold-out validation are used to train and build the ResNet based FDD model, while the testing set is regarded as unknown new data used to evaluate the generalization performance of the established FDD model.

To further evaluate the advantage of the proposed ResNet based FDD method, two others commonly used deep learning structures are used for comparison, including fully connected convolution neural network (CNN) and convolutional auto-encoder (CAE). In view of fair comparison, the CNN and CAE models are trained and tested by the same way as the proposed ResNet based model. Specifically, the CNN structure is designed with the 8 fully connected convolution layers, two max-polling layers and one linear classifier, and the CAE structure is composed of four convolution layers, four de-convolution layers and one linear classifier. Both of the CNN and CAE models are trained, using the same Adam training algorithm as illustrated in Fig. 10 and the same hyper-parameters as listed in Table 7.

The training and testing results for CAE, CNN and ResNet based FDD models on the simulated dataset are given in Table 9, where best results are highlighted in bold. In addition, a radar chart and Receiver

Operating Characteristic (ROC) curves are plotted in Fig. 12 to illustrate the comparison result of the specific and overall testing accuracy of three different FDD models. From Table 9 and Fig. 13, it is demonstrated that the proposed ResNet based FDD model achieves the highest training and testing accuracy in all the cases. The proposed ResNet based FDD model achieve the perfect training accuracy up to 100% and the testing accuracy nearly up to 100% except the case of Degradation 1. In comparison to ResNet based model, although both of CNN and CAE models achieve the training and testing accuracy up to 100% in the cases of the Shading 2 and Short Circuit 1, the accuracies are not high enough in the cases of other faults. For example, the training and testing accuracies of the CNN model are 92.37% and 92.39% respectively in the case of the Shading 3, and the training and testing accuracies of the CNN model are just 59.57% and 61.39% respectively in the case of the Open Circuit fault. To further analyze the performance of the proposed ResNet based FDD model, the classification confusion matrix for the testing set is plotted in Fig. 14 to visualize not only the accuracy of the classifier but also the predicted types of the misdiagnosed faults. As can be observed in Fig. 14, there are only two simulated PVS degradation samples are misdiagnosed to be the Shading 3 fault.

To test and compare the reliability, the proposed deep learning based FDD models are trained and tested independently for 20 times. Then, statistical analysis is carried out on the average accuracy of FDD

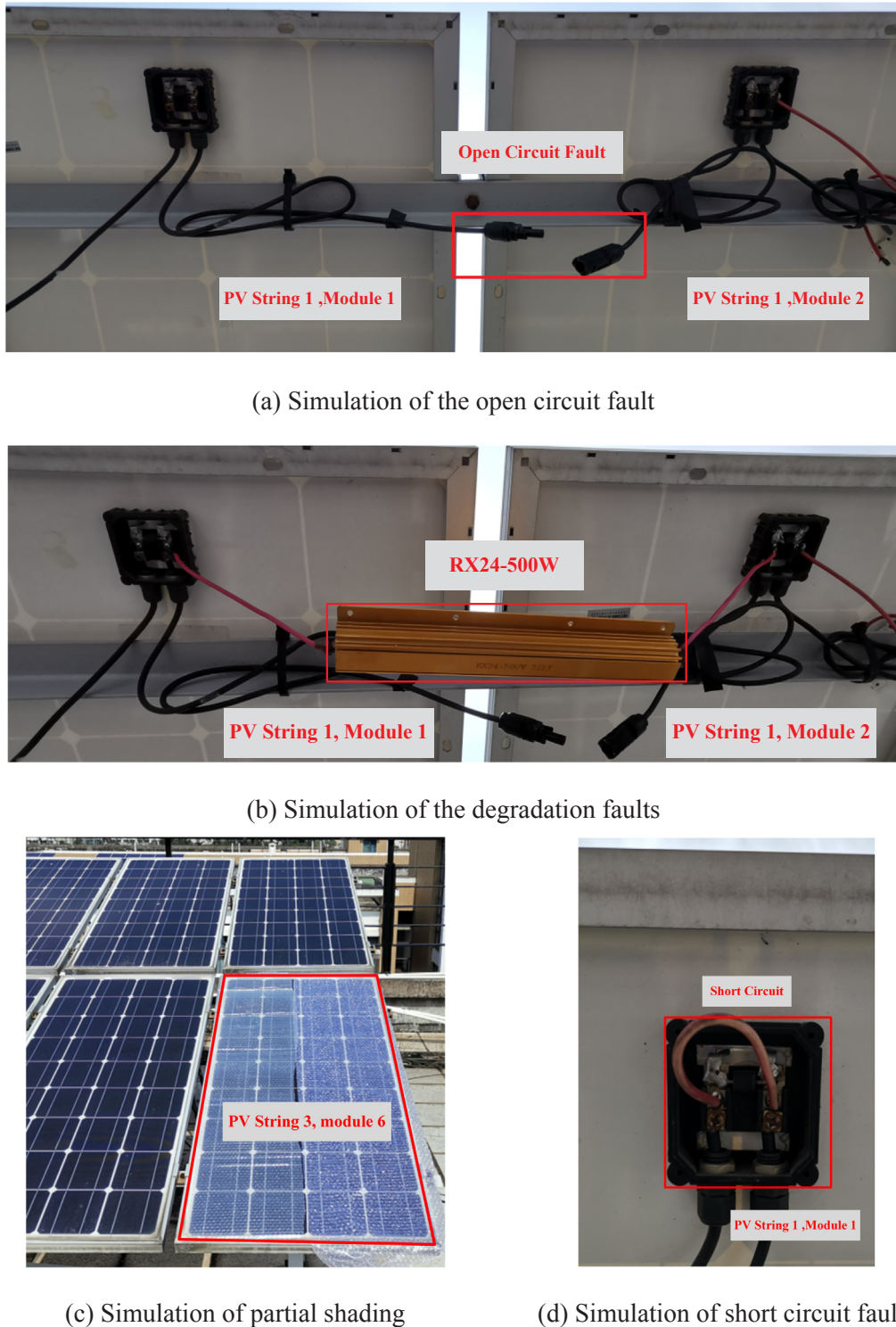


Fig. 17. Experimental setting for faults simulation on the real PV array.

models, and the results are listed in Table 10, where the Max represents maximum, Min represents minimum, Std denotes standard deviation, and the best results are in bold. Especially, the Std can be used as a criterion to evaluate the stability of the models. Obviously, the proposed ResNet has achieved the best result in both of two datasets. Specifically, it is validated that the ResNet has the highest generalization performance and accuracy as indicated by the highest average accuracy in both of the training and testing sets (99.955% and 99.94% respectively). In terms of the stability, the proposed ResNet has a

standard deviation of only 0.001 among 20 independent runs, which is much lower than that of the CNN (0.003 for training set and 0.004 for testing set) and CAE (0.042 for training set and 0.044 for testing set). From the aforementioned results, it can be observed that the performance of the proposed ResNet model is slightly better than the CNN model, while both of them are much better than the CAE model on the simulation dataset.

To further verify the training efficiency, the loss function convergence of the ResNet based and CNN based FDD models during the

Table 11

Distribution of the experimental data samples.

Fault Types	Type Number	Number of samples			
		Training set	Hold-out	Validation	Testing set
Normal	1	403	47	191	
Shading 1	2	297	34	142	
Shading 2	3	79	9	39	
Shading 3	4	92	10	44	
Degradation 1	5	177	20	85	
Degradation 2	6	226	26	109	
Short Circuit 1	7	196	22	94	
Short Circuit 2	8	171	20	83	
Open Circuit	9	229	27	110	
Totally		1870	215	897	

training are further examined and compared. In Fig. 15, the convergence curves of two models' loss function in training processes are compared, from which it is obvious that the proposed ResNet model converges much faster than the CNN model, and the final convergence loss of the ResNet model is much lower than that of the CNN model as well. Therefore, the ResNet based FDD model is validated to be better than the CNN based model in terms of the training efficiency as well.

4.2. Real experiments and result analysis

In order to further verify the feasibility and performance of the proposed ResNet based FDD method in real applications, some real fault experiments are performed on the actual PV array consisting of eighteen GL-100 monocrystalline silicon PV modules with a power peak of 18 kW. As illustrated in Fig. 16(a), the laboratory PV array consists of three parallel-connected PV strings with six PV modules in series, which is marked by red frame. In order to measure the output I-V characteristic curves of the PV array and corresponding ambient conditions, a commercial I-V tester (Model: PROVA101) is used in the experiment, which is manufactured by the TES Electrical Electronic Crop. As shown in Fig. 16(b) and (c), the I-V tester consists of a main I-V tester and a wireless sensor with Bluetooth communication. The wireless sensor is mounted on the same plane as the PV module to measure the incident irradiance and the back-panel temperature of a PV module, as shown in Fig. 16(b). The main I-V tester is portable and can be placed in convenient places, as shown in Fig. 16(c). The I-V tester can be configured to automatically measure the output I-V curves and corresponding ambient conditions of the PV array in a specified time interval, which greatly facilitate the fault experiments.

The faults simulation approaches for the real PV array are illustrated in Fig. 17, which are the same as the Simulink based fault models for the PV array, as detailed in subsection 2.2. Specifically, the open-circuit fault is simply emulated by disconnecting a PV module in the PV string as shown in Fig. 17(a). The Degradation1 fault is emulated by adding a high-power resistor of 3Ω in series with a PV string as shown in

Fig. 17(b). Similarly, Degradation 2 fault is emulated by inserting the same high-power resistor in series with the output of the PV array. The Shading1 fault is emulated by covering a PV module with an acrylic board, as shown in Fig. 17(c). Correspondingly, the Shading2 and Shading3 faults are emulated with 2 and 3 PV shaded PV modules respectively. As shown in Fig. 17(d), the Short Circuit 1 fault is emulated by short-circuiting one PV module in a PV string. The Short Circuit 2 is emulated by short-circuiting 2 PV modules in one string.

The fault experiments were carried out with the aforementioned configuration on some consecutive days. Each case of the fault experiment was performed in a whole day to cover a relative large ambient conditions. Due to the uncontrollable ambient conditions and limitation of the I-V tester (it needs almost half minute to scan a I-V), some abnormal I-V curves unrelated to the faults are excluded from the dataset. After excluding the abnormal I-V curves, there are just around 3000 effective experimental data samples collected in total. In comparison to the simulation dataset, the quality and number of the data samples in the real dataset is much lower, which poses great challenge on the FDD model. The 70% of total data samples of each operating condition are randomly selected as training set and the remaining 30% samples are used for testing. The specific distribution of real data samples is detailed in the Table 11. It can be observed that the number of data samples for nine cases of operating conditions is not identical, which may cause performance decrease on the trained FDD models.

Similar to the simulation study, three different deep learning models, including the CNN, CAE and ResNet, are trained, tested and compared on the same experimental dataset. The training and testing results of the three models are listed in Table 12 where the highest accuracy is marked in bold, and the radar chart and ROC curve of the accuracy are plotted in Fig. 18. It can be observed in the Table 12 and Fig. 18 that the proposed ResNet model achieves the best performance in terms of both the training accuracy and testing accuracy for most of the cases (except the testing accuracies of the Shading 3 and Open Circuit faults). Furthermore, the proposed ResNet model achieves very high training and testing accuracy for all the cases (all of the accuracies are higher than 92.31%, most of the accuracies are up to 100%), and it is much better than the other two models that perform poor in some cases, such as Shading 2 and Degradation 1. Therefore, compared to the results of the simulation experiment, the proposed ResNet FDD model achieves a very competitive performance.

To analyze the detailed classification result of the testing set, the confusion matrix the proposed ResNet model is plotted in Fig. 19, from which it can be observed the average correct and false classification rates of the proposed fault detection model are up to 98.1% and 1.9% respectively. The main types of misdiagnosed faults are the Shading 2, Shading 3, Degradation 1, Degradation 2 and Open circuit.

In order to test and compare the reliability, the three FDD models are trained and tested for 20 times independently. Similar to the simulation study, Table 13 lists the statistical result of the overall average training and testing accuracies of the three models in the 20 random runs, in which the best results are highlighted in bold as well. In

Table 12

Comparison of the classification accuracy on the experimental dataset.

Item	CNN		CAE		ResNet	
	Training Accuracy (%)	Testing Accuracy (%)	Training Accuracy (%)	Testing Accuracy (%)	Training Accuracy (%)	Testing Accuracy (%)
Normal	95.04	93.19	90.82	86.91	100.0	100.0
Shading 1	98.68	99.30	95.29	96.48	100.0	100.0
Shading 2	24.05	15.38	58.23	48.72	100.0	92.31
Shading 3	95.65	81.82	100.0	100.0	99.95	97.73
Degradation 1	94.92	91.76	50.28	51.76	100.0	95.29
Degradation 2	99.56	96.33	87.17	88.99	100.0	96.33
Short Circuit 1	90.82	92.55	72.96	67.02	99.49	100.0
Short Circuit 2	100.0	98.80	93.57	93.98	100.0	100.0
Open Circuit	100.0	100.0	93.01	90.00	100.0	95.45

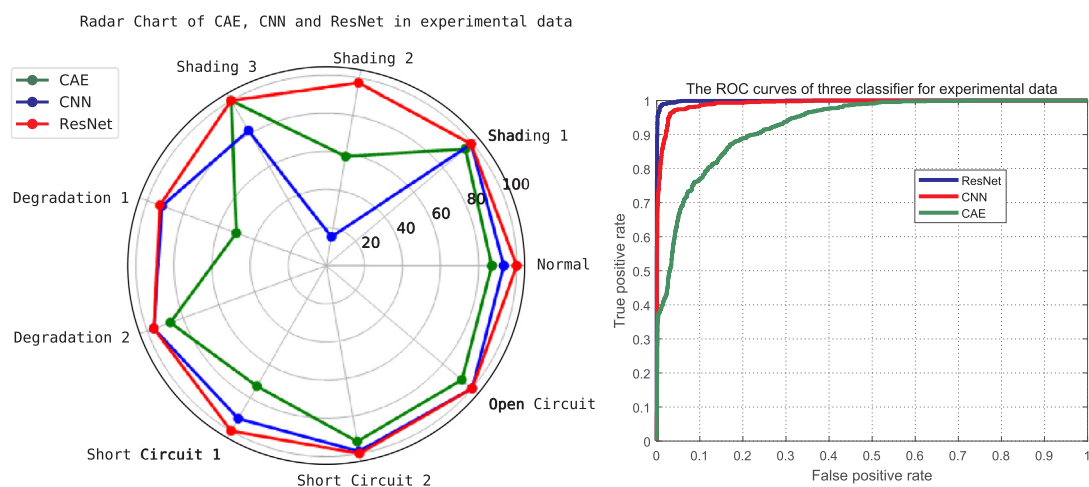


Fig. 18. Accuracy comparison among the three models on the same real dataset.

Confusion Matrix											
Output Class	1	2	3	4	5	6	7	8	9		
	1	191 21.3%	0 0.0%	0 0.0%	0 0.0%	1 0.1%	1 0.1%	0 0.0%	0 0.0%	2 0.2%	97.9% 2.1%
	2	0 0.0%	142 15.8%	1 0.1%	0 0.0%	0 0.0%	0 0.0%	0 0.0%	0 0.0%	0 0.0%	99.3% 0.7%
	3	0 0.0%	0 0.0%	36 4.0%	1 0.1%	0 0.0%	0 0.0%	0 0.0%	0 0.0%	0 0.0%	97.3% 2.7%
	4	0 0.0%	0 0.0%	1 0.1%	43 4.8%	0 0.0%	0 0.0%	0 0.0%	0 0.0%	0 0.0%	97.7% 2.3%
	5	0 0.0%	0 0.0%	0 0.0%	0 0.0%	81 9.0%	3 0.3%	0 0.0%	0 0.0%	3 0.3%	93.1% 6.9%
	6	0 0.0%	0 0.0%	0 0.0%	2 0.2%	105 11.7%	0 0.0%	0 0.0%	0 0.0%	0 0.0%	98.1% 1.9%
	7	0 0.0%	0 0.0%	1 0.1%	0 0.0%	1 0.1%	0 0.0%	94 10.5%	0 0.0%	0 0.0%	97.9% 2.1%
	8	0 0.0%	0 0.0%	0 0.0%	0 0.0%	0 0.0%	0 0.0%	83 9.3%	0 0.0%	0 0.0%	100% 0.0%
	9	0 0.0%	0 0.0%	0 0.0%	0 0.0%	0 0.0%	0 0.0%	0 0.0%	105 11.7%	0 0.0%	100% 0.0%
100% 0.0%											
92.3% 7.7%											
97.7% 2.3%											
95.3% 4.7%											
96.3% 3.7%											
100% 0.0%											
95.5% 4.5%											
98.1% 1.9%											

Fig. 19. The confusion matrix of the testing accuracy of the ResNet model on real dataset.

Table 13
Statistical comparison of average classification accuracy on real dataset.

Algorithm	Accuracy (%)	Statistical analysis of the accuracies in 20 random runs			
		Max	Min	Mean	Std
CAE	Training set	74.866	40.963	58.964	0.121
	Testing set	73.244	37.124	56.452	0.130
CNN	Training set	96.898	65.829	86.431	0.115
	Testing set	95.318	61.204	83.431	0.115
ResNet	Training set	99.947	91.497	98.463	0.029
	Testing set	98.774	88.852	95.778	0.036

Table 13, it can be observed that the ResNet based FDD model achieve the best result in terms of all the statistical variables, in comparison to the CNN and CAE based FDD models. Specifically, the statistical mean average training and testing accuracy of the proposed ResNet model are

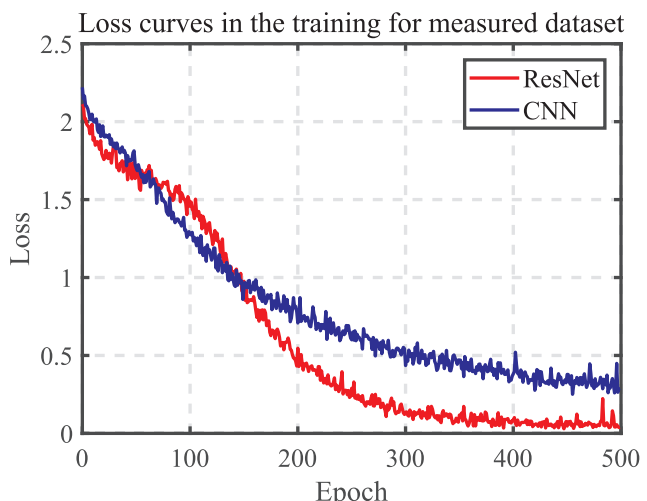


Fig. 20. Comparison of loss curves of ResNet and CNN models on real dataset.

as high as 98.463% and 95.778. Especially, the standard deviation of the ResNet is as low as 0.029 and 0.036 for training and testing sets respectively and are much lower than those of the CNN and CAE, which validates that the proposed ResNet based FDD model features highest reliability in real dataset as well. In addition, by comparing the results in Tables 13 and 10, it is obvious that the statistical accuracy of the proposed ResNet model on real dataset is very competitive to that on simulated dataset as well.

To verify and compare the training efficiency between the two best models (ResNet and CNN), their convergence curves of the loss function during the training are plotted in Fig. 20. It can be observed that the ResNet model converges much faster than the CNN model especially at the end of the training, and it finally reaches a much lower loss value. Therefore, the ResNet model is validated to be more efficient than the CNN model again in terms of the training efficiency on the real dataset.

4.3. Discussion of the advantage and limitation

This subsection mainly discusses the advantage and limitation of the proposed method in comparison to the common threshold based FDD methods. From the data perspective, the proposed ResNet based FDD method relies on static I-V curves and corresponding ambient irradiance and temperature to realize the accurate and fine detection and diagnosis of common early faults of a PV array, whilst most threshold based methods use real-time data of dynamic operating points.

Obviously, the entire I-V curves contain much more complete information than the single data point, from which the fault status can be better detected and distinguished. In addition, the dynamic points are commonly assumed to be the maximum power points (MPP), which is usually not the real case. In fact, the operating points are affected by the dynamic MPPT algorithms and fluctuates around the real MPP points determined by the varying ambient condition. Therefore, we argue that the I-V curve would be more accurate and reliable. However, the I-V curves are difficult to be obtained online by common commercial inverters, even if some of the commercial inverters features capability. Therefore, the proposed method is more suitable for offline FDD of PV arrays using an I-V curve tester. Instead, the common threshold based FDD methods are simple, efficient and appropriate for online operation.

From the algorithm perspective, as a kind of machine learning based methods, the proposed method would require a predetermined dataset to train and establish the FDD model. Therefore, the proposed method would need the costly human effort to collect data samples of faults, but it can build the accurate FDD model from the dataset automatically and objectively. Instead, the common threshold based FDD methods rely on rigorous analysis and extraction of fault indicators and threshold and manual determination of the FDD procedure, which is expert-dependent and may be limited on the accuracy and generalization performance. In terms of the computation complexity, although the proposed ResNet based FDD method requires complex computation to build the FDD model, it can be deployed and run efficiently on common low power embedded platforms, since they have enough computation resource. In contrast, the threshold based FDD methods are simple, hence they can be run in much simpler and cheaper embedded platforms.

5. Conclusions

In this study, based on output I-V characteristic curves and input ambient condition data, a novel deep residual network (ResNet) based intelligent fault detection and diagnosis (FDD) approach is proposed to detect different types and levels of common early faults of PV array, including partial shading, degradation, short circuit and open circuit faults. Firstly, raw measured I-V characteristics curves of normal and fault conditions are down-sampled and combined with irradiance and temperature to form two-dimensional data samples. Secondly, a new ResNet structure is proposed as the FDD model, which consists of residual blocks, convolutional layers, average pooling layers and linear classifier. Lastly, the adaptive moment estimation learning algorithm is used to train the ResNet based model using the acquired datasets.

An accurate Simulink based simulation model is designed for a laboratory PV array to verify the proposed ResNet based FDD model, based on which simulation and real fault experiments are performed to obtain simulation and real experimental fault data samples under various ambient conditions. Both of simulation and real experiments results validate the high accuracy and generalization performance of the proposed method. In the case of simulation study, the average training and testing accuracy of the established ResNet model in 20 random runs are up to 99.995% and 99.940% respectively. In the case of real study, the average training and testing accuracies are 98.463% and 95.778% accordingly, which are just slightly lower than those of the simulation. Moreover, the standard deviation of the accuracy is in the order of 1E-3 for the simulation case and 1E-2 for the real case, which validates the high stability of the ResNet model as well.

Two other popular deep learning models trained by the same datasets are used for comparison to validate of the advantage of the proposed ResNet based model, including convolution neural network and convolutional auto-encoder. Both of the simulation and real experimental comparison results demonstrate that the proposed ResNet based model achieve the best overall performance in terms of the accuracy, generalization performance, stability and training efficiency.

The proposed ResNet based FDD method is promising to be integrated into I-V testing systems for PV arrays and the PV inverters with

I-V curve scanning capability to realize efficient and automatic fault detection and diagnosis.

Declaration of Competing Interest

The authors declare that they have no known competing financial interests or personal relationships that could have appeared to influence the work reported in this paper.

Acknowledgments

The authors would like to acknowledge the financial supports in part from the National Natural Science Foundation of China (Grant Nos. 61601127 and 61574038), the Fujian Provincial Department of Science and Technology of China (Grant Nos. 2019H0006 and 2018J01774), and the Foundation of Fujian Provincial Department of Industry and Information Technology of China (Grant No. 82318075).

References

- [1] I. Pvps, 2018 SNAPSHOT OF GLOBAL PHOTOVOLTAIC MARKETS; 2018.
- [2] Madeti SR, Singh S. A comprehensive study on different types of faults and detection techniques for solar photovoltaic system. *Sol Energy* 2017;158:161–85.
- [3] Pillai DS, Prasanth Ram J, Rajasekar N, Mahmud A, Yang Y, Blaabjerg F. Extended analysis on line-line and line-ground faults in PV arrays and a compatibility study on latest NEC protection standards. *Energy Convers Manage* 2019. X, p. 100009, 2019/04/23/.
- [4] Silvestre S, Kichou S, Chouder A, Nofuentes G, Karatepe E. Analysis of current and voltage indicators in grid connected PV (photovoltaic) systems working in faulty and partial shading conditions. *Energy* 2015;86:42–50.
- [5] Dhone A, Sharma R, Saha TK. PV module degradation analysis and impact on settings of overcurrent protection devices. *Sol Energy* 2018;160:360–7.
- [6] Akram MN, Lotfifard S. Modeling and health monitoring of DC side of photovoltaic array. *IEEE Trans Sustainable Energy* 2015;6(4):1245–53.
- [7] Xiong Q, et al. Arc fault detection and localization in photovoltaic systems using feature distribution maps of parallel capacitor currents. *IEEE J Photovoltaics* 2018;8(4):1090–7.
- [8] Bressan M, Gutierrez A, Garcia Gutierrez L, Alonso C. Development of a real-time hot-spot prevention using an emulator of partially shaded PV systems. *Renewable Energy* 2018;127:334–43.
- [9] Barbato M, Barbato A, Meneghini M, Tavernaro G, Rossetto M, Meneghesso G. Potential induced degradation of N-type bifacial silicon solar cells: an investigation based on electrical and optical measurements. *Sol Energy Mater Sol Cells* 2017;168:51–61.
- [10] Dhimish M, Holmes V, Mather P. Novel photovoltaic micro crack detection technique. *IEEE Trans Device Mater Reliab* 2019.
- [11] Alam MK, Khan F, Johnson J, Flicker J. A comprehensive review of catastrophic faults in PV arrays: Types, detection, and mitigation techniques. *IEEE J Photovoltaics* 2015;5(3):982–97.
- [12] Mellit A, Tina G, Kalogirou S. Fault detection and diagnosis methods for photovoltaic systems: a review. *Renew Sustain Energy Rev* 2018;91:1–17.
- [13] Triki-Lahiani A, Bennani-Ben Abdellah A, Slama-Belkhodja I. Fault detection and monitoring systems for photovoltaic installations: a review. *Renew Sustain Energy Rev* 2018;82, pp. 2680–2692, 2018/02/01/.
- [14] Gallardo-Saavedra S, Hernández-Callejo I, Duque-Perez O. Technological review of the instrumentation used in aerial thermographic inspection of photovoltaic plants. *Renew Sustain Energy Rev* 2018;93:566–79.
- [15] Bedrich KG, et al. Quantitative electroluminescence imaging analysis for performance estimation of PID-influenced PV modules. *IEEE J Photovoltaics* 2018;8(5):1281–8.
- [16] Takashima T, Yamaguchi J, Ishida M. Disconnection detection using earth capacitance measurement in photovoltaic module string. *Prog Photovoltaics Res Appl* 2008;16(8):669–77.
- [17] Roy S, Alam MK, Khan F, Johnson J, Flicker J. An irradiance independent, robust ground fault detection scheme for PV arrays based on spread spectrum time domain reflectometry (SSTDR). *IEEE Trans Power Electron* 2017.
- [18] Yi Z, Etemadi A. Line-to-line fault detection for photovoltaic arrays based on multi-resolution signal decomposition and two-stage support vector machine. *IEEE Trans Ind Electron* 2017.
- [19] Takashima T, Yamaguchi J, Otani K, Oozeki T, Kato K, Ishida M. Experimental studies of fault location in PV module strings. *Sol Energy Mater Sol Cells* 2009;93(6–7):1079–82.
- [20] Pillai DS, Blaabjerg F, Rajasekar N. A comparative evaluation of advanced fault detection approaches for PV systems. *IEEE J Photovolt* 2019.
- [21] Chen Z, et al. Random forest based intelligent fault diagnosis for PV arrays using array voltage and string currents. *Energy Convers Manage* 2018;178:250–64.
- [22] Tadj M, Benmouiza K, Cheknane A, Silvestre S. Improving the performance of PV systems by faults detection using GISTEL approach. *Energy Convers Manage* 2014;80(80):298–304.
- [23] Silvestre S, Silva MAD, Chouder A, Guasch D, Karatepe E. New procedure for fault

- detection in grid connected PV systems based on the evaluation of current and voltage indicators. *Energy Convers Manage* 2014;86:241–9.
- [24] Saleh KA, Hooshyar A, El-Saadany EF, Zeineldin HH. Voltage-based protection scheme for faults within utility-scale photovoltaic arrays. *IEEE Trans Smart Grid* 2017.
- [25] Gokmen N, Karatepe E, Silvestre S, Celik B, Ortega P. An efficient fault diagnosis method for PV systems based on operating voltage-window. *Energy Convers Manage* 2013;73:350–60.
- [26] Khoshnami A, Sadeghkhani I. Two-stage power-based fault detection scheme for photovoltaic systems. *Sol Energy* 2018;176:10–21. 2018/12/01.
- [27] Chaibi Y, Malvoni M, Chouder A, Boussetta M, Salhi M. Simple and efficient approach to detect and diagnose electrical faults and partial shading in photovoltaic systems. *Energy Convers Manage* 2019;196:330–43.
- [28] Madeti SR, Singh S. Online modular level fault detection algorithm for grid-tied and off-grid PV systems. *Sol Energy* 2017;157:349–64.
- [29] Dhimish M, Holmes V, Mehrdadi B, Dales M, Chong B, Zhang L. Seven indicators variations for multiple PV array configurations under partial shading and faulty PV conditions. *Renewable Energy* 2017;113:438–60.
- [30] Wang W, Liu A, Chung H, Lau RW. Fault diagnosis of photovoltaic panels using dynamic current-voltage characteristics. *IEEE Trans Power Electron* 2016;31(2):1.
- [31] Bressan M, El Basri Y, Galeano A, Alonso C. A shadow fault detection method based on the standard error analysis of IV curves. *Renew Energy* 2016;99:1181–90.
- [32] Garoudja E, Harrou F, Sun Y, Kara K, Chouder A, Silvestre S. Statistical fault detection in photovoltaic systems. *Sol Energy* 2017;150:485–99.
- [33] Harrou F, Taghezouti B, Sun Y. Robust and flexible strategy for fault detection in grid-connected photovoltaic systems. *Energy Convers Manage* 2019;180. pp. 1153–1166. 2019/01/15/.
- [34] Dhimish M, Holmes V, Dales M. Parallel fault detection algorithm for grid-connected photovoltaic plants. *Renew Energy* 2017;113:94–111.
- [35] Chen L, Wang X. Adaptive fault localization in photovoltaic systems. *IEEE Trans Smart Grid* 2017.
- [36] Kumar BP, Ilango GS, Reddy MJB, Chilakapati N. Online fault detection and diagnosis in photovoltaic systems using wavelet packets. *IEEE J Photovoltaics* 2018;8(1):257–65.
- [37] Kang B-K, Kim S-T, Bae S-H, Park J-W. Diagnosis of output power lowering in a PV array by using the Kalman-filter algorithm. *IEEE Trans Energy Convers* 2012;27(4):885–94.
- [38] Youssef A, El-Telbany M, Zekry A. The role of artificial intelligence in photo-voltaic systems design and control: a review. *Renew Sustain Energy Rev* 2017;78:72–9.
- [39] Benkercha R, Moulahoum S. Fault detection and diagnosis based on C4. 5 decision tree algorithm for grid connected PV system. *Sol Energy* 2018;173:610–34.
- [40] Chine W, Mellit A, Lugh Vi, Malek A, Sulligoi G, Massi Pavan A. A novel fault diagnosis technique for photovoltaic systems based on artificial neural networks. *Renew Energy* 2016;90:501–12.
- [41] Jufri FH, Oh S, Jung J. Development of photovoltaic abnormal condition detection system using combined regression and support vector machine. *Energy* 2019.
- [42] Chen Z, Wu L, Cheng S, Lin P, Wu Y, Lin W. Intelligent fault diagnosis of photovoltaic arrays based on optimized kernel extreme learning machine and I-V characteristics. *Appl Energy* 2017;204:912–31. 2017/10/15/.
- [43] Garoudja E, Chouder A, Kara K, Silvestre S. An enhanced machine learning based approach for failures detection and diagnosis of PV systems. *Energy Convers Manage* 2017;151:496–513.
- [44] Zhao Y, Ball R, Mosesian J, de Palma J-F, Lehman B. Graph-based semi-supervised learning for fault detection and classification in solar photovoltaic arrays. *IEEE Trans Power Electron* 2015;30(5):2848–58.
- [45] Lin P, Lin Y, Chen Z, Wu L, Chen L, Cheng S. A density peak-based clustering approach for fault diagnosis of photovoltaic arrays. *Int J Photoenergy* 2017;2017.
- [46] Liu G, Zhu L, Wu X, Wang J. Time series clustering and physical implication for photovoltaic array systems with unknown working conditions. *Sol Energy* 2019;180:401–11. 2019/03/01/.
- [47] Zhu H, Lu L, Yao J, Dai S, Hu Y. Fault diagnosis approach for photovoltaic arrays based on unsupervised sample clustering and probabilistic neural network model. *Sol Energy* 2018;176:395–405. 2018/12/01/.
- [48] Liu S, Dong L, Liao X, Hao Y, Cao X, Wang X. A dilation and erosion-based clustering approach for fault diagnosis of photovoltaic arrays. *IEEE Sens J* 2019.
- [49] Yi Z, Etemadi AH. Fault detection for photovoltaic systems based on multi-resolution signal decomposition and fuzzy inference systems. *IEEE Trans Smart Grid* 2017;8(3):1274–83.
- [50] Dhimish M, Holmes V, Mehrdadi B, Dales M, Mather P. Photovoltaic fault detection algorithm based on theoretical curves modelling and fuzzy classification system. *Energy* 2017;140:276–90.
- [51] Liu S, Dong L, Liao X, Cao X, Wang X. Photovoltaic array fault diagnosis based on Gaussian Kernel Fuzzy C-means clustering algorithm. *Sensors* 2019;19(7):1520.
- [52] Belaout A, Krim F, Mellit A, Talbi B, Arabi A. Multiclass adaptive neuro-fuzzy classifier and feature selection techniques for photovoltaic array fault detection and classification. *Renew Energy* 2018;127:548–58. 2018/11/01/.
- [53] Liu W, Wang Z, Liu X, Zeng N, Liu Y, Alsaadi FE. A survey of deep neural network architectures and their applications. *Neurocomputing* 2017;234:11–26.
- [54] Schmidhuber J. Deep learning in neural networks: an overview. *Neural Networks* 2015;61:85–117.
- [55] Khan S, Yairi T. A review on the application of deep learning in system health management. *Mech Syst Sig Process* 2018;107:241–65.
- [56] Wen L, Li X, Gao L, Zhang Y. A new convolutional neural network-based data-driven fault diagnosis method. *IEEE Trans Ind Electron* 2018;65(7):5990–8.
- [57] Xu L, Cao M, Song B, Zhang J, Liu Y, Alsaadi FE. Open-circuit fault diagnosis of power rectifier using sparse autoencoder based deep neural network. *Neurocomputing* 2018;311:1–10.
- [58] Shao H, Jiang H, Zhang H, Liang T. Electric locomotive bearing fault diagnosis using a novel convolutional deep belief network. *IEEE Trans Ind Electron* 2018;65(3):2727–36.
- [59] Li X, Yang Q, Lou Z, Yan W. Deep learning based module defect analysis for large-scale photovoltaic farms. *IEEE Trans Energy Convers* 2019;34(1):520–9.
- [60] Appiah AY, Zhang X, Ayawli BBK, Kyeremeh F. Long short-term memory networks based automatic feature extraction for photovoltaic array fault diagnosis. *IEEE Access* 2019;7:30089–101.
- [61] Rawat W, Wang Z. Deep convolutional neural networks for image classification: a comprehensive review. *Neural Comput* 2017;29(9). pp. 2352–2449. 2017/09/01.
- [62] He K, Zhang X, Ren S, Sun J. Deep Residual Learning for Image Recognition. presented at the 2016 IEEE Conference on Computer Vision and Pattern Recognition (CVPR), Las Vegas, NV, United States; 2015.
- [63] Zhao M, Kang M, Tang B, Pecht M. Deep residual networks with dynamically weighted wavelet coefficients for fault diagnosis of planetary gearboxes. *IEEE Trans Ind Electron* 2018;65(5):4290–300.
- [64] Chen Z, Chen Y, Wu L, Cheng S, Lin P, You L. Accurate modeling of photovoltaic modules using a 1-D deep residual network based on I-V characteristics. *Energy Convers Manage* 2019;186:168–87. 2019/04/15/.
- [65] Chen Z, Wu L, Lin P, Wu Y, Cheng S. Parameters identification of photovoltaic models using hybrid adaptive Nelder-Mead simplex algorithm based on eagle strategy. *Appl Energy* 2016;182(2016):47–57.
- [66] Abbassi R, Abbassi A, Jemli M, Chebbi S. Identification of unknown parameters of solar cell models: a comprehensive overview of available approaches. *Renew Sustain Energy Rev* 2018;90:453–74.
- [67] Wu L, et al. Parameter extraction of photovoltaic models from measured I-V characteristics curves using a hybrid trust-region reflective algorithm. *Appl Energy* 2018;232C:36–53.
- [68] Fadhel S, et al. PV shading fault detection and classification based on IV curve using principal component analysis: application to isolated PV system. *Sol Energy* 2019;179:1–10.
- [69] Ioffe S, Szegedy C. “Batch Normalization: Accelerating Deep Network Training by Reducing Internal Covariate Shift,” presented at the Proceedings of the 32nd International Conference on International Conference on Machine Learning – Volume 37, Lille, France; 2015.
- [70] Krizhevsky A, Sutskever I, Hinton GE. ImageNet Classification with Deep Convolutional Neural Networks. In International Conference on Neural Information Processing Systems; 2012.
- [71] Simonyan K, Zisserman A. Very deep convolutional networks for large-scale image recognition. *Comput Sci* 2014.
- [72] D.P. Kingma J. Ba Adam: A method for stochastic optimization *Comput Sci* 2014.
- [73] Glorot X, Bengio Y. Understanding the difficulty of training deep feedforward neural networks. *J Mach Learn Res* 2010;9:249–56.